The Influence of Helicity on Numerically Simulated Convective Storms

KELVIN K. DROEGEMEIER AND STEVEN M. LAZARUS

School of Meteorology and Center for Analysis and Prediction of Storms, University of Oklahoma, Norman, Oklahoma

ROBERT DAVIES-JONES

National Severe Storms Laboratory, NOAA, Norman, Oklahoma

(Manuscript received 11 May 1992, in final form 18 December 1992)

ABSTRACT

A three-dimensional numerical cloud model is used to investigate the influence of storm-relative environmental helicity (SREH) on convective storm structure and evolution, with a particular emphasis on the identification of ambient shear profiles that are conducive to the development of long-lived, strongly rotating storms. Eleven numerical simulations are made in which the depth and turning angle of the ambient vertical shear vector are varied systematically while maintaining a constant magnitude of the shear in the shear layer. In this manner, an attempt is made to isolate the effects of different environmental helicities on storm morphology and show that the SREH and bulk Richardson number, rather than the mean shear in the low levels, determine the rotational characteristics and morphology of deep convection.

The results demonstrate that storms forming in environments characterized by large SREH are longer-lived than those in less helical surroundings. Further, it appears that the storm-relative winds in the layer 0–3 km must, on average, exceed 10 m s^{-1} over most of the lifetime of a convective event to obtain supercell storms. The correlation coefficient between vertical vorticity ζ and vertical velocity w, which (according to linear theory of dry convection) should be proportional to the product of the normalized helicity density, NHD (i.e., relative helicity), and a function involving the storm-relative wind speed, has the largest peak values (in time) in those simulated storms exhibiting large SREH and strong storm-relative winds in the low levels. Even when the vorticity is predominantly streamwise in the storm-relative framework, giving a normalized helicity density near unity (as is the case in many of these simulations), significant updraft rotation and large w–ζ correlation coefficients do not develop and persist unless the storm-relative winds are sufficiently strong.

The correlation coefficient between w and ζ based on linear theory is found to be a significantly better predictor of net updraft rotation than the bulk Richardson number (BRN) or the BRN shear, and slightly better than the 0–3-km SREH. Both the theoretical correlation coefficient and the SREH are based on the motion of the initial storm after its initially rapid growth. Linear theory also predicts correctly the relative locations of the buoyancy, vertical velocity, and vertical vorticity extrema within the storms after allowance is made for the effects of vertical advection. In predicting the maximum vertical vorticity both above and below 1.14 km, rather than the actual w–ζ correlation, the 0–3-km SREH performs slightly worse than the BRN. The correlation coefficient, SREH, and BRN all do a credible job of predicting storm type. Thus, it is recommended that operational forecasters use the BRN to predict storm type because it is independent of storm motion, and the SREH to characterize the rotational properties of storms once their motions can be established.

Finally, the ability of the NHD to characterize storm type and rotational properties is examined. Computed using the storm-relative winds, the NHD shows little ability to predict storm rotation (i.e., maximum w–ζ correlation and maximum vertical vorticity), because it neglects the magnitudes of the vorticity and storm-relative wind vectors. Histograms of the *disturbance* NHD show a distinct bias toward positive values near unity for supercell storms, indicating an extraction of helicity from the mean flow by the disturbance, and only a slight bias for multicell storms.

1. Introduction

a. Determination of storm characteristics

Observations have shown that environments possessing moderate to high buoyancy and ample shear tend to produce distinctly severe convective modes known as supercell storms (e.g., Browning 1964; Marwitz 1972a; Klemp 1987). Associated with these storms are a number of characteristic features, including a propensity for steadiness and longevity (storm lifetimes of two hours or more), a principal intense and cyclonically rotating updraft, large hail, and well-defined regions of rotation known as mesocyclones that, in many cases, spawn tornadoes. The origin of midlevel updraft rotation in such storms results from the presence of environmental streamwise vorticity in the lowest few kilometers of the atmosphere (Davies-Jones 1984 and references therein).

Corresponding author address: Prof. Kelvin K. Droegemeier, School of Meteorology, University of Oklahoma, Sarkeys Energy Center Rm. 1310, 100 East Boyd, Norman, OK 73019.

Despite some ambiguity in the classification of convective storms, the possibility of predicting storm type (e.g., supercell, multicell, squall line, single cell) based on a few observable quantities has long been a desirable goal. Using a three-dimensional numerical model, Weisman and Klemp (1982; hereafter WK82) attacked this problem for a unidirectionally sheared environment by evaluating the combined influence of vertical wind shear and buoyancy on convective storm morphology. In their study, available buoyancy was measured by the convective available potential energy (CAPE), which is defined as the vertically integrated positive thermal buoyancy of a parcel rising from the surface:

$$\text{CAPE} = g \int \frac{\theta(z) - \bar{\theta}(z)}{\bar{\theta}(z)}\, dz, \qquad (1)$$

where g is the acceleration due to gravity, $\theta(z)$ is the potential temperature of a surface parcel undergoing dry and then moist-adiabatic ascent, $\bar{\theta}(z)$ is the potential temperature of the environment, and the integration is performed only over that portion of the vertical column where the parcel is positively buoyant (i.e., the positive area on a thermodynamic diagram).

To quantify the relative effects of buoyant instability and vertical shear, WK82 used a nondimensional parameter, known as the bulk Richardson number (BRN), to categorize numerically simulated convection according to storm longevity, intensity, and other observed features. The BRN is defined as

$$\text{BRN} = \frac{\text{CAPE}}{0.5(\bar{u}^2 + \bar{v}^2)}, \qquad (2)$$

where $\bar{u}$ and $\bar{v}$ are the components of the difference between the density-weighted mean winds over the lowest 6 km and the lowest 500 m. The BRN represents only a gross estimate of the effects of vertical wind shear on convection since it fails to account fully for either hodograph shape (i.e., the turning of the environmental shear vector with height) or the magnitude of the storm-relative winds, particularly in the low levels (0–3 km) (see section 6 and Lazarus and Droegemeier 1990). Nevertheless, it has proved more than adequate for distinguishing among storm types, as WK82 and Weisman and Klemp (1986, hereafter WK86) showed that modeled supercells are likely when $5 \leqslant \text{BRN} \leqslant 50$, and that modeled multicells generally occur when BRN > 35. (Note the overlap in these ranges.)

The turning of the shear vector with height (or hodograph curvature) is known to have a profound influence on storm structure (e.g., Wilhelmson and Klemp 1978; Rotunno and Klemp 1982). In an extension to their earlier work, Weisman and Klemp (1984, hereafter WK84) included the effects of directionally varying wind shear on modeled storm evolution. The results of those experiments, in which the hodograph turned clockwise through 180° at a constant rate in the lowest 5 km, showed a preference for updraft development on the right flank of the storm system and a tendency for supercell development on the right flank and suppression of multicell storms on the left flank with increasing hodograph radius (i.e., decreasing BRN). Large correlations between vertical velocity and vertical vorticity, especially after two hours of integration, were found for the right-flank storms in the high-shear experiments, indicating that the presence of large environmental vorticity leads to increased storm rotation through the tilting and stretching of vortex tubes. However, because the shear vector in each of the WK84 hodographs turned through the same angle overall, issues relating to the impact of hodograph shape on storm morphology could not be addressed.

The coexistence of supercells and multicells within the same simulation in the WK84 study, with the updrafts of the former developing more slowly at first, indicates that storm type and motion are not determined solely by the environmental hodograph (or the BRN). Indeed, WK84 (p. 2497) recommended monitoring storm motion (relative to that of nearby cells), in addition to using information about the storm environment and cell evolution within the overall storm system, to distinguish supercells from other types of storms. Our results confirm this as an appropriate strategy, and suggest that storm motion, which may be influenced by environmental inhomogeneities such as boundary-layer convergence lines (e.g., Weaver 1979), plays an important role in determining storm type. Further, storm motion and rotation are often interlinked (e.g., Davies-Jones 1984).

Rasmussen and Wilhelmson (1983) and Davies (1989) used the magnitude of the mean shear, computed as the sum (over a layer 2 or 4 km deep) of the shear magnitudes across each 200-m sublayer divided by the depth of the layer, in conjunction with the CAPE to predict the occurrence of mesocyclones and tornadoes. Although both studies found that large *mean shear* (in the layer 0–4 km in the former study, and 0–4 km and 0–2 km in the latter) and high instability were correlated with tornadic activity, neither considered the effects of hodograph shape because by definition *the mean shear measures only the cumulative distance between successive points on a hodograph without regard to how the shear vector turns with height.* Further, the length of a (fractal) hodograph is an ill-defined quantity because it increases with finer and finer measurement resolution (Davies-Jones et al. 1990; see also Mandelbrot 1983, 25–33). The results presented herein suggest that at least two distinctive storm types (multicells and supercells) are in fact possible for environments having initially identical thermodynamic profiles and 0–2-km mean shears, and that the vertical shear profile and storm motion play key roles in convective morphology, particularly storm persistence and the development of rotation.

b. Helicity

The study of persistent entities in fluid systems is not intrinsic to meteorology; the characteristics of long-lived features in turbulent flow have been thoroughly documented in fluid mechanics (e.g., Lesieur 1990). Kraichnan (1973) and André and Lesieur (1977) suggested that helicity, defined as the volume integral of the scalar product of velocity and vorticity, may inhibit the downscale cascade of energy in homogenous, isotropic turbulence. The helicity $\mathscr{H}$ is defined as

$$\mathscr{H} = \int_{\Omega} H d\Omega = \int_{\Omega} \mathbf{v} \cdot \omega d\Omega, \tag{3}$$

where H is the helicity density, Ω the volume of integration, $\mathbf{v}$ the velocity vector, and ω the vorticity vector ($=\nabla \times \mathbf{v}$). In contrast to vorticity, which is a fundamental measure of microscopic rotation within a fluid, helicity provides for a topological interpretation of inviscid barotropic flows in terms of linkages of vortex lines (e.g., Moffatt and Tsinober 1992). In the absence of baroclinicity and viscosity, and in a domain with rigid boundaries at which the normal component of the vorticity vanishes, $\mathscr{H}$ is a volume-conserved quantity for incompressible flow. In the case of a Beltrami flow, in which the velocity and vorticity vectors are everywhere aligned, the stretching and tilting terms in the vector vorticity equation are exactly balanced by the advection terms. Consequently, the cascade of energy from large to small scales is blocked, thereby eliminating the energy loss experienced by energy-containing scales. In supercell storms, where the velocity and vorticity vectors are not perfectly aligned and buoyancy forces are, of course, important, the cascade is only inhibited.

Inspired by the aforementioned studies, Lilly (1983, 1986a,b) hypothesized that thunderstorms characterized by large helicity (i.e., supercells) are less susceptible to dissipation and thus are longer-lived, and possess a more monolithic structure, than their nonhelical counterparts. Although turbulence dynamicists are beginning to doubt the role of helicity in the preservation of coherent structures in boundary layers (e.g., Pelz et al. 1986; Kerr 1987; Wallace and Balint 1990), certain measures involving helicity do have some relevance to thunderstorm dynamics. Indeed, Davies-Jones et al. (1990) suggested that the storm-relative environmental helicity (hereafter SREH) over an appropriately defined inflow depth (e.g., 3 km) can be used to forecast the rotational characteristics of thunderstorms (see also Woodall 1990). Here, the SREH is defined as

$$\mathscr{H}_v = \int_{0\text{ km}}^{3\text{ km}} [(\mathbf{V} - \mathbf{C}) \cdot \omega] dz, \tag{4}$$

where $\mathbf{C}$ is the storm motion vector, $\omega = \mathbf{k} \times d\mathbf{V}/dz$, and the subscript v distinguishes this measure of helicity (vertical integral only, because the integrand is horizontally invariant) from the formal definition given by Eq. (3). [Note that since helicity is not Galilean invariant, it is appropriately defined in the storm's frame of reference: Davies-Jones (1984); Davies-Jones et al. (1990); Lilly (1990).] The parameter $\mathscr{H}_v$ was chosen by Davies-Jones et al. (1990) because of its dependence on both the streamwise vorticity (Davies-Jones 1984) and strength of the storm-relative winds. [The importance of strong storm-relative inflow has also been recognized in other studies, e.g., Wilhelmson and Klemp (1978), WK82, and Brooks et al. (1993).] As defined by Eq. (4), $\mathscr{H}_v$ has a simple graphical interpretation as minus twice the signed area swept out by the storm-relative wind vector between two levels on a wind hodograph (see the Appendix). Thus, unlike the mean shear, $\mathscr{H}_v$ is insensitive to the fine structure (fractal nature) of the wind distribution. Davies-Jones et al. estimated that $\mathscr{H}_v \approx 157\ \text{m}^2\ \text{s}^{-2}$, which is equivalent to 90° of veering of the storm-relative wind vector coupled with a storm-relative inflow magnitude of 10 m s^{-1}, represents an approximate lower threshold for the occurrence of mesocyclones. Further, they demonstrated a correlation between $\mathscr{H}_v$ and tornado intensity.

Using proximity soundings, McCaul (1991) investigated the severity of tornado outbreaks in hurricanes as a function of the local environment and found strong shear in the lowest 1 km in the closest soundings. More specifically, he examined the CAPE, BRN, BRN shear [the denominator in Eq. (2)], $\mathscr{H}_v$, normalized helicity density (or relative helicity—see sections 4 and 6b), and storm-relative streamwise vorticity in an effort to establish ties between the intensity of the outbreaks and the ambient environment. Because the motion of individual cells was generally unknown, McCaul estimated it as the mean wind between the surface and 6 km, a rough approximation that generally leads to underestimates of true helicities for tornadic storms (McCaul 1987). All of the purely dynamic parameters were found to exhibit significant correlations with tornado outbreak severity, and to correctly predict the right front quadrant of the hurricane as the favored region for tornado formation. For the ten closest proximity soundings, $\mathscr{H}_v$ was found to average 234 m^2 s^{-2}. In contrast, CAPE values were low, uncorrelated with outbreak severity, and were largest in the left rear quadrant. Thus, the BRN was found to be a poorer predictor than the purely dynamic parameters.

Davies-Jones (1984) employed linear theory to show that the covariance between the vertical velocity and vertical vorticity, which is a measure of helical convection, should depend upon the strength of the storm-relative winds in addition to the streamwise vorticity. The likelihood of mesocyclones is rather low when the storm-relative winds are too weak, nominally less than 10 m s^{-1}. Our results suggest that supercell development is unlikely when the magnitude of the storm-relative wind falls below a critical value even in the

presence of strong storm-relative directional shear. Brooks et al. (1993) reached a similar conclusion, and in their supercell simulations found that, given moderate to high values of SREH, the strength of the *surface* storm-relative wind (18 m s^{-1} or higher) determined whether the storms developed long-lived mesocyclones at low levels.

As described in more detail in section 4, Davies-Jones et al. (1984) adapted the linear theory formula for the correlation coefficient between vertical velocity and vertical vorticity (Davies-Jones 1984) so that it could be evaluated from a sounding and observed or predicted storm motion. They suggested a correlation coefficient of 0.5 as a threshold for mesocyclone formation.

c. *The present study*

Although these and other studies have provided valuable insight into relationships among storm evolution, type, and the ambient environment, there remain important unexplored questions regarding the role of helicity in storm dynamics, particularly its ability to characterize storm type and rotation. The present work addresses these and related issues through a set of numerical simulations designed to examine the influence of hodograph shape and environmental helicity on storm structure and evolution, with a particular emphasis on the identification of ambient wind profiles that are conducive to the development of long-lived, rotating storms. Employing the Klemp and Wilhelmson (1978) three-dimensional cloud model, we present results of 11 model integrations in which *we vary systematically the depth of the shear layer and the hodograph turning angle while maintaining a constant shear magnitude.* In this manner we isolate the effects of different environmental helicities—which are, of course, partly determined by storm motion—on storm morphology. Although large ambient shear is necessary for the development of thunderstorm rotation, our results suggest that the SREH plays an important role in defining the nature and rotational characteristics of convection. Of the 11 simulations, an admittedly small sample from which sweeping generalizations should be avoided, 4 produce supercells and 7 produce multicells.

We discuss in section 2 the methodology of the numerical experiments, while in section 3 we classify the simulations based on the modes of convection produced, and examine two representative cases. Section 4 presents a comparison of our results with linear theory of dry convection, and section 5 addresses the effects of the storm-relative winds on storm characteristics. We evaluate in section 6 the potential usefulness of the SREH, normalized helicity density, the theoretical correlation coefficient between vertical velocity and vertical vorticity, and BRN shear as tools for forecasting storm rotation and longevity. Frequency distributions of disturbance normalized helicity density are evaluated in section 7, and a summary of our findings and their possible implications for storm predictability are presented in section 8.

2. Methodology

The simulations are conducted using the three-dimensional cloud model of Klemp and Wilhelmson (1978), including modifications implemented by Wilhelmson and Chen (1982). The thermodynamic profile used in each experiment is identical to the analytical sounding employed by WK82, and is slightly subadiabatic in the lowest kilometer with a surface mixing ratio of 15 g kg^{-1}. The CAPE of this sounding is approximately 2500 J kg^{-1}. The computational domain extends 60 km in both the east–west and north–south directions, with a horizontal grid spacing of 1 km. Using the grid-stretching formulation described by Wilhelmson and Chen (1982), the vertical grid spacing varies continuously from 127 m near the surface to approximately 1 km at the domain top (15 km). Each simulation is run for 2 h, with all fields saved at 5-min intervals for subsequent analysis.

Convection is initiated by positioning a positively buoyant thermal impulse in the boundary layer (see Klemp and Wilhelmson 1978). The computational domain is translated at a constant velocity (determined for each experiment by trial and error) to ensure that the principal features of interest remain as far away from the lateral boundaries as possible. A complete listing of relevant model physical and computational parameters is provided in Table 1.

In order to isolate the effects of hodograph curvature on storm morphology, we systematically vary the base-state wind speed and rate of turning with height to produce hodographs that turn through a quarter circle, half circle, three-quarter circle, and full circle over

TABLE 1. Physical and computational parameters used in the simulation experiments.

Parameter	Symbol	Value
Large time step	Δt	6.0 s
Small time step	$\Delta\tau$	1.5 s
Coriolis parameter	f	10^{-4} s^{-1}
Intrinsic gravity-wave phase speed	C_*	30 m s^{-1}
Nondimensional surface drag coefficient	C_d	0.00
Turbulent Prandtl number	K_m/K_h	1/3
Fourth-order horizontal mixing coefficient	K_4	10^9 m^4 s^{-1}
Second-order vertical mixing coefficient	K_2	$100 \leq K_2 \leq 1000$ m^2 s^{-1}
Initial thermal disturbance:		
Magnitude	$\Delta\theta$	2.0 K
Horizontal radius	x_r, y_r	10 km
Vertical radius	z_r	1.4 km
Height of center above ground	z_c	1.4 km

depths of 2, 4, and 8 km (Fig. 1). The winds *above* the shear layer in each experiment are constant and are equal to the value at the *top* of the layer. The magnitude of the environmental vorticity ($=7.85 \times 10^{-3}$ s^{-1}) is constant across the shear layer in each experiment, and is the same for all hodographs; only the depth of the shear layer and the rate at which the vorticity vector changes direction with height varies among the exper-

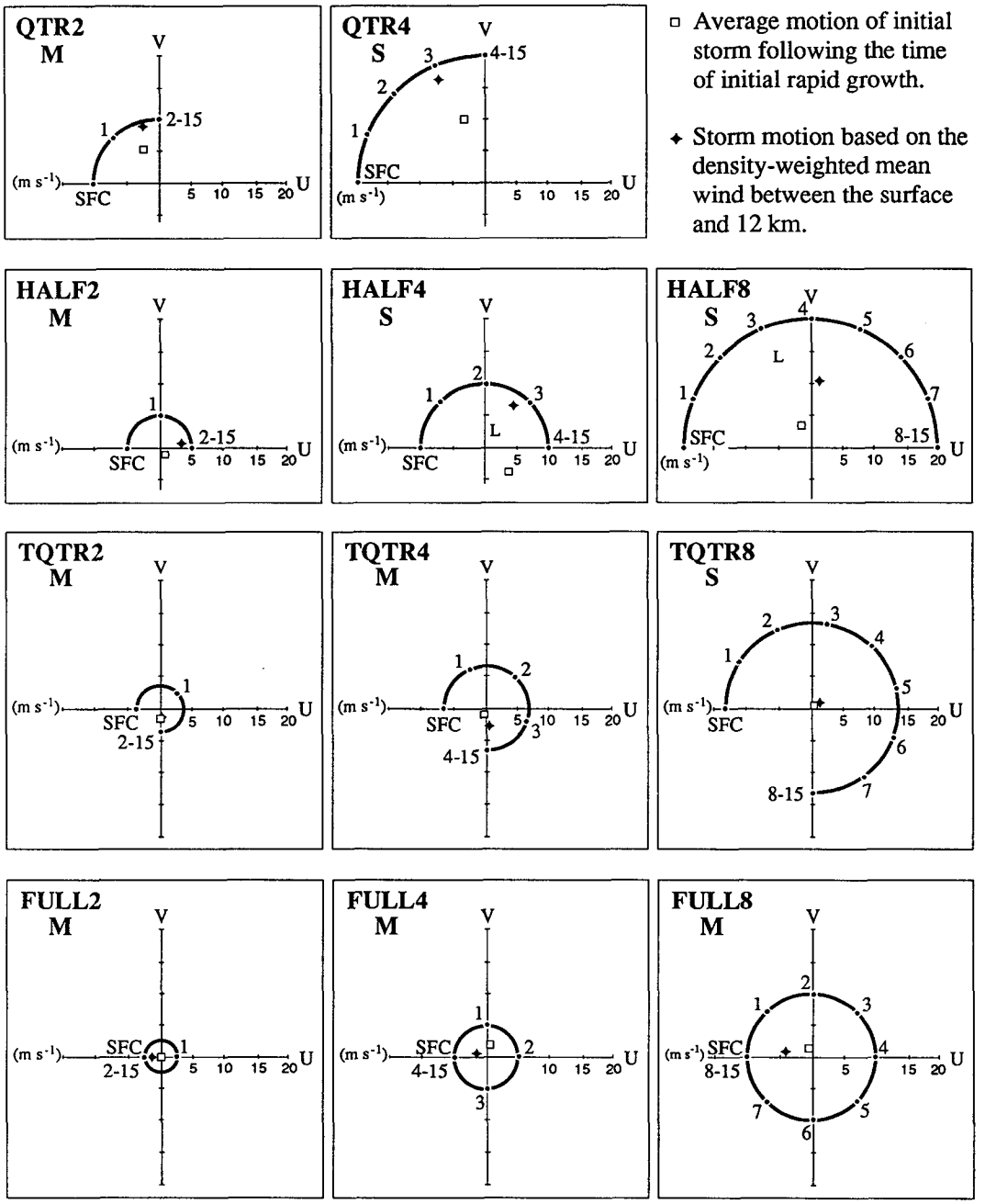

FIG. 1. Base-state wind hodographs (m s^{-1}), each having the same shear magnitude in the shear layer, used in the model simulations. The numbers along each curve indicate the altitude (km). The dominant storm type for each simulation is indicated by M and S for multicell and supercell, respectively, and the abbreviations QTR, HALF, TQTR, and FULL indicate turning angles of 90°, 180°, 270°, and 360°, respectively, for the base-state ground-relative winds. The number appended to each abbreviation indicates the depth of the shear layer (km). Storm motions are depicted as indicated, and L denotes the average motion of the split-off left mover associated with the initial storm in experiments HALF4 and HALF8. In experiment TQTR2, the symbol depicting the actual storm motion nearly overlays that associated with the 0–12-km mean wind.

iments (see the Appendix). Thus, the environmental mean shear is also the same for each initial hodograph *over the depth for which the shear is nonzero.*

It is important in the discussion that follows to distinguish between the terms *curvature* and *turning* as applied to wind hodographs. The former describes the degree to which a hodograph possesses a curved shape (i.e., the mathematical definition of curvature), while the latter is related to the angle subtended by two *storm-relative* wind vectors at different heights. Thus, for example, a storm propagating to the right of a perfectly straight hodograph (rectilinear shear) can exhibit considerable turning of the storm-relative winds with height despite the absence of curvature in the hodograph.

A consequence of stipulating a constant shear magnitude is that the hodograph radius R in our experiments increases (decreases) as the shear-layer depth χ increases (decreases) or the total turning angle β decreases (increases) (see the Appendix). The hodograph radius is given by $R = 2.5\chi\pi/\beta$, where R is given in meters per second, χ in kilometers, and β in radians. Consequently, hodographs possessing large amounts of turning have relatively small radii (large curvature) and thus produce storms that encounter relatively weak storm-relative winds, unless the shear layer is quite deep. Although the hodographs used in this study are admittedly somewhat idealized, they are appropriate because we seek not to reproduce a particular observed storm but rather to isolate the general effects of vertical shear on storm morphology.

To simplify the identification of all experiments, we use the convention that QTRχ, HALFχ, TQTRχ, and FULLχ represent hodographs that turn through a quarter, half, three-quarter, and full circle, respectively; for example, HALF4 represents turning through a half circle over the layer 0–4 km. Due to numerical difficulties associated with intense, localized cooling in the stratosphere above the top of the storm, QTR8 was not performed successfully.

3. General storm characteristics

In order to establish the basic characteristics of the 11 simulations, we show the maximum updraft speed of the initial storm for each experiment as a function of shear-layer depth and hodograph shape in Table 2. In general, the strongest initial updrafts tend to be associated with the shallowest shear layers and small-radii hodographs. The former characteristic is due to the propensity for updrafts to grow more vigorously in the absence of deep ambient shear, while the latter relates to the type of shear present. That is, because the shear vector veers substantially (is more unidirectional) with height in small- (large-) radii hodographs, the associated initial updrafts are less (more) tilted and are thus relatively intense (weak).

Based on interpretations of storm structure and morphology, we have classified the simulated convection into two categories: supercells (S) and multicells (M) (see Fig. 1). The convection associated with supercell simulations is relatively long-lived and exhibits persistent rotating updrafts positioned above the low-level gust front. In addition, hooklike features are typically present in the rainwater fields at low levels. Simulations classified as multicell generally exhibit rapidly growing, intense initial updrafts that often rotate early in their life cycle but dissipate fairly rapidly. Subsequent short-lived cells (e.g., lifetimes on the order of 30 min or less) form along rapidly expanding surface outflows and rotate less strongly than, and more briefly than, the initial updrafts. It is important to note that none of our modeled multicells exhibit the organized repetitive cell development and decay described by Browning (1962), Marwitz (1972b), and Browning et al. (1976).

The dominant convective mode for each simulation, shown in Table 3, agrees well with the BRN predictions suggested by WK84 and Fig. 15.18 of WK86. In our set of simulations, all four supercells and all of the multicells except for FULL8 are predicted unambiguously by the BRN. Note that storms in experiment QTR2 are primarily multicellular in nature even though the BRN for this environment is just outside the range of overlap between supercells and multicells. We believe that multicells occur in this simulation because the rather weak, low-level storm-relative winds allow the gust front to propagate well away from the base of the main updraft, thereby blocking its principal supply of unstable air. Although FULL8 is classified as a multicell, it exhibits longer periods of rotation than its counterparts, with low-level vorticity reaching 2.55 $\times 10^{-2}$ s^{-1} at 45 min into the simulation. From Tables 2 and 3, it is evident that the maximum updraft speed of the initial storm *generally* increases with increasing BRN. Since we do not vary the CAPE in these experiments, this result is consistent with Fig. 14a of WK84.

More detailed information on the simulated storms is provided in Figs. 2 and 3, which show time series of the domain-maximum vertical velocity and ground-relative updraft positions at 5-min intervals, respectively. The latter are determined by tracking the location of individual updrafts at $z = 3$ km until they either dissipate or merge with other storms. Figures 2a

TABLE 2. Maximum updraft speed (m s^{-1}) of the initial storm in all experiments.

Hodograph shape	Shear layer (km) 0–2	0–4	0–8
Quarter circle (QTR)	59.2	49.7	N/A
Half circle (HALF)	60.6	55.5	56.3
Three-quarter circle (TQTR)	61.2	58.1	54.9
Full circle (FULL)	61.3	60.6	55.3

TABLE 3. Bulk Richardson number (BRN), computed using Eq. (2), of the initial environment for each simulation. Storm type is indicated by M for multicell and S for supercell.

Hodograph shape	Shear layer (km) 0–2	0–4	0–8
Quarter circle (QTR)	53 (M)	20 (S)	N/A
Half circle (HALF)	89 (M)	33 (S)	18 (S)
Three-quarter circle (TQTR)	252 (M)	90 (M)	25 (S)
Full circle (FULL)	2034 (M)	399 (M)	41 (M)

and 3a–d indicate that the initial storms in the 2-km shear-layer experiments show a general trend of decreasing intensity with time after initially rapid growth, though individual short-lived cells along the expanding gust fronts contribute to temporary reintensifications (e.g., HALF2). The multicells in these four simulations show no degree of organization, and in fact exhibit widely varying motions depending upon the depth of the updraft and the propagation of the surface cold pool (e.g., the initial storm in QTR2 moves to the north-northwest, while a weaker secondary storm to its east moves northward initially and then eastward along with the eastern gust front).

In sharp contrast to the above, the initiating disturbance in QTR4 (Figs. 2b and 3e) produces a relatively steady, long-lived, and intense supercell storm that propagates toward the northwest before 60 min and to the north thereafter, with weak secondary convection

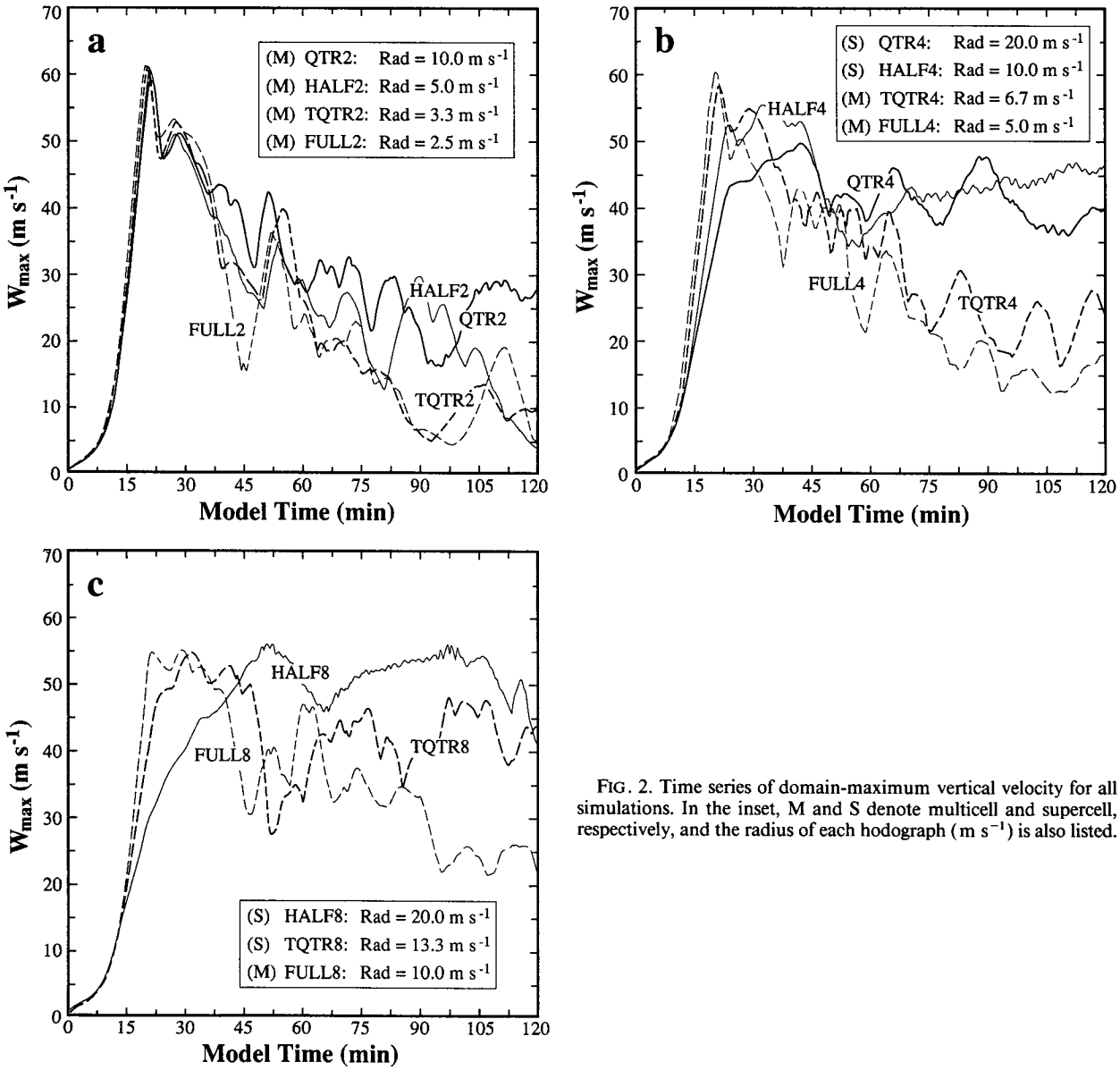

FIG. 2. Time series of domain-maximum vertical velocity for all simulations. In the inset, M and S denote multicell and supercell, respectively, and the radius of each hodograph (m s^{-1}) is also listed.

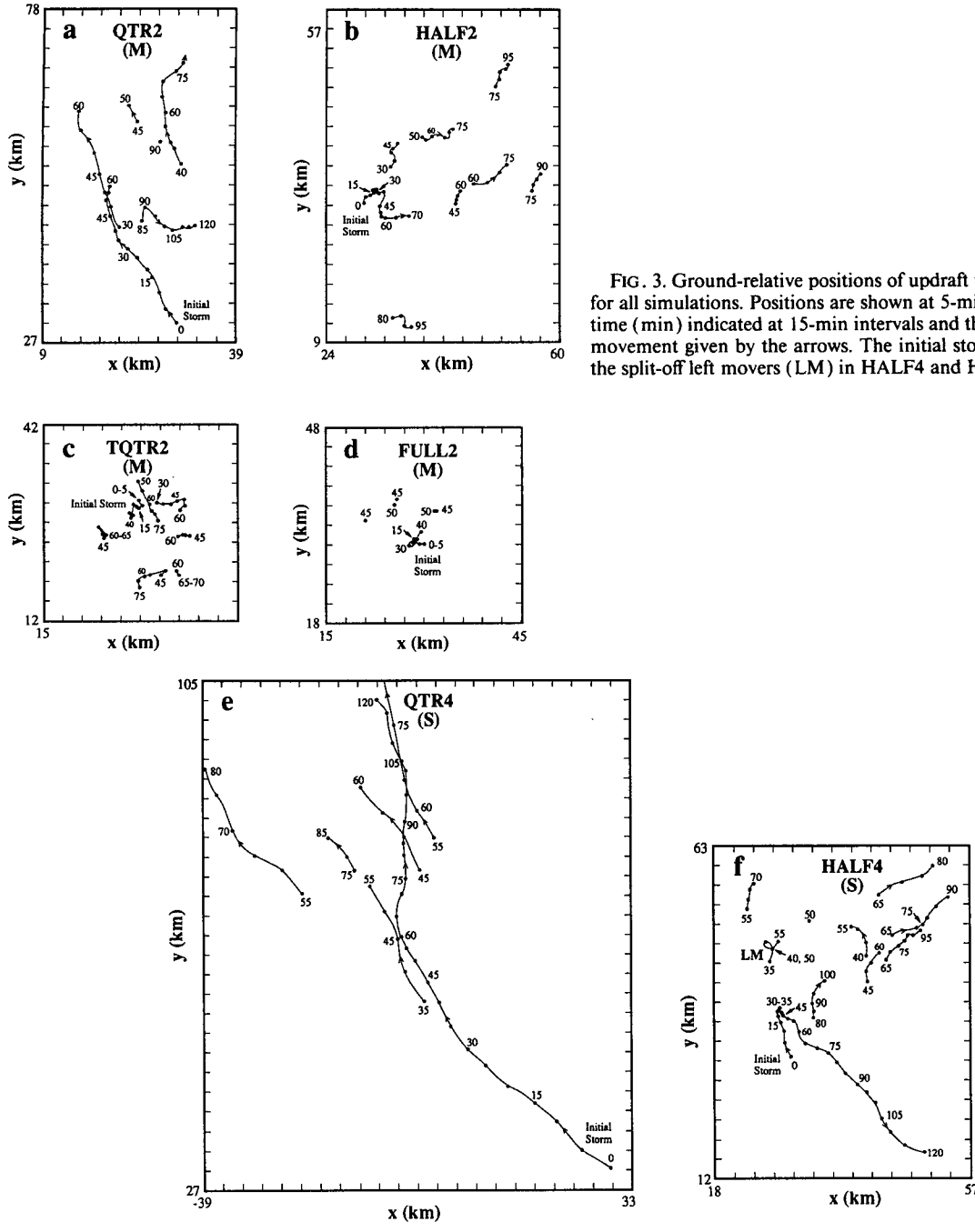

FIG. 3. Ground-relative positions of updraft maxima at $z = 3$ km for all simulations. Positions are shown at 5-min intervals, with the time (min) indicated at 15-min intervals and the direction of storm movement given by the arrows. The initial storm is labeled, as are the split-off left movers (LM) in HALF4 and HALF8.

developing nearby (one cell of which splits off from, and moves to the left of, the parent storm). A similar evolution is observed in HALF4 (Fig. 3f), though as described further below, this storm changes direction rather markedly between 30 and 40 min as the surface cold pool becomes established and begins to expand in lateral extent. Note that, although the supercell in HALF4 propagates toward the southeast after 40 min, most storms forming to the northeast of it move in a northeasterly direction. It is interesting that storms forming in TQTR4 and FULL4 (Figs. 2b and 3g,h) are distinctly weaker, less organized, and show a trend of decreasing updraft intensity with time relative to those in the other 4-km shear-layer experiments. We attribute these characteristics to weak low-level (0–3 km) storm-relative inflow, which—as shown later—is a critical parameter in determining storm longevity and rotational characteristics.

As one might anticipate considering the radii and shape of each hodograph, storms in the 8-km shear-

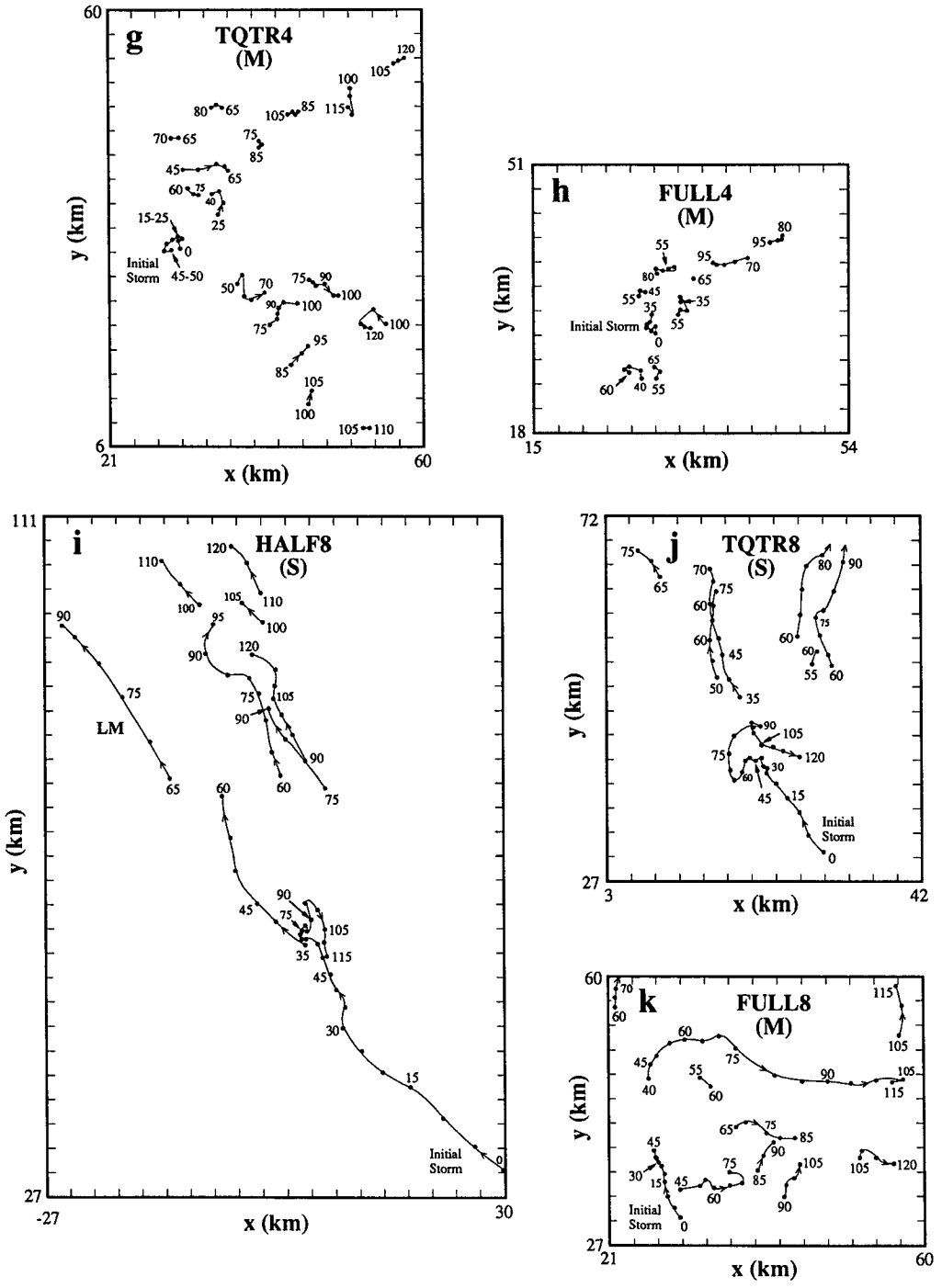

FIG. 3. (*Continued*)

layer experiments (Figs. 2c and 3i–k) are among the strongest, with the initiating storms in HALF8 and TQTR8 exhibiting clear supercell characteristics, and interestingly, virtually reversing their direction of motion between 70 and 90 min as the principal updraft begins to follow the expanding gust front. Note that, although the supercell updrafts ultimately become more steady than their multicell counterparts, they develop more slowly at first. The TQTR4 and FULL8 simulations (Fig. 2) produce multicell storms that decline more slowly and attain higher values of vertical vorticity than the other multicells (see discussion below). In fact, FULL8 (Fig. 3k) may be viewed as a storm that falls just short of becoming a supercell.

The clear and sometimes dramatic disparity in motion illustrated above for modeled storms developing in close proximity to one another has been documented observationally (e.g., Newton and Fankhauser 1964), and illustrates the difficulty involved in predicting a priori the motion of a given convective event based solely on the environment. Because storm motion is necessary for computing the SREH (and thus for using it to forecast certain storm properties, sections 4–6), it must be either observed or predicted from the environment. We compare in Fig. 1 an estimate of storm motion, based upon the density-weighted mean of the base-state wind from the surface to 12 km, with the motion of the initial storm in each simulation. The latter is computed as an average, over the life of the storm excluding the first 20 min of rapid development and erratic movement, of the position of the maximum updraft at $z = 3$ km. *Hereafter, we refer to this quantity as the "storm motion" unless otherwise qualified.* The observed and predicted storm motions show good agreement for the more circular hodographs (e.g., TQTR and FULL), while in the other cases, the 0–12-km mean wind tends to overestimate the actual storm speed. (The 0–6-km mean wind was evaluated as well, but proved to be a poorer estimator.) One reason that the mean wind is not a precise predictor of storm motion is that it neglects the influence of the surface cold pool, as documented further below.

Focusing now on the detailed structure of two representative simulations, HALF4 (supercell) and QTR2 (multicell), we note first that the initiating disturbance in HALF4 produces an especially intense and long-lived storm (Figs. 4a and 5a) that moves along with the expanding gust front toward the southeast, *outside* the semicircular area defined by the hodograph (see also Fig. 1). This motion enhances significantly the storm-relative winds in the lowest 3 km and, as discussed further below, increases the SREH by increasing the area swept out by the storm-relative wind vectors between 0 and 3 km. As the storm continues to travel southeastward along with—though slightly behind—the gust front (Fig. 4a), a mesocyclone develops beneath the base of the main updraft and intensifies throughout the simulation (evidenced partly by the kink in the gust front), producing low-level (below 1.14 km) vertical vorticity in excess of 2.2 $\times 10^{-2}$ s^{-1} (Fig. 6a). By the end of the 2-h integration, this supercell shows no signs of weakening. A companion storm is initiated along the gust front to the northeast of the main supercell and is clearly evident

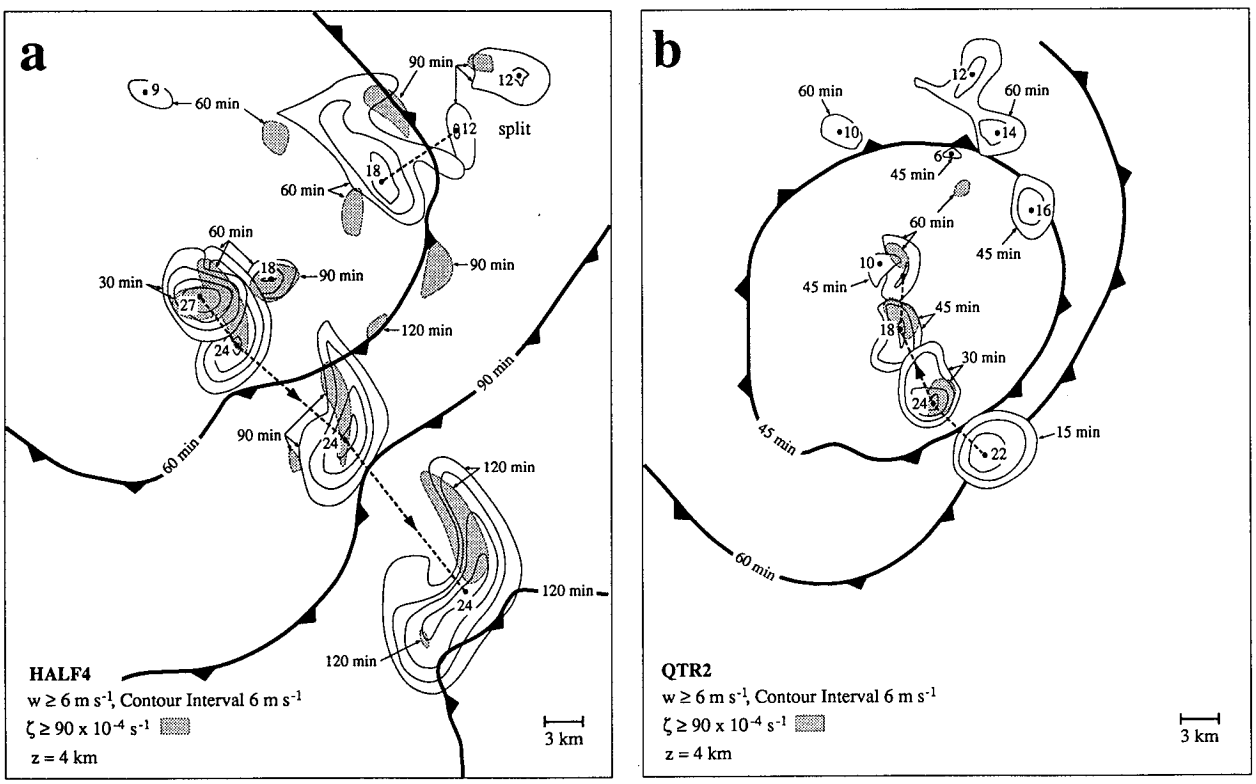

FIG. 4. Storm histories for experiments (a) HALF4 (supercell) and (b) QTR2 (multicell). Updrafts at $z = 4$ km are shown by thin solid lines (contour interval of 6 m s^{-1}, first contour of 6 m s^{-1}) with the maximum value indicated (m s^{-1}), vertical vorticity ζ exceeding 90 $\times 10^{-4}$ s^{-1} is enclosed by stippling, and the surface gust-front position is depicted by thick barbed lines. Times are indicated in minutes next to each major feature.

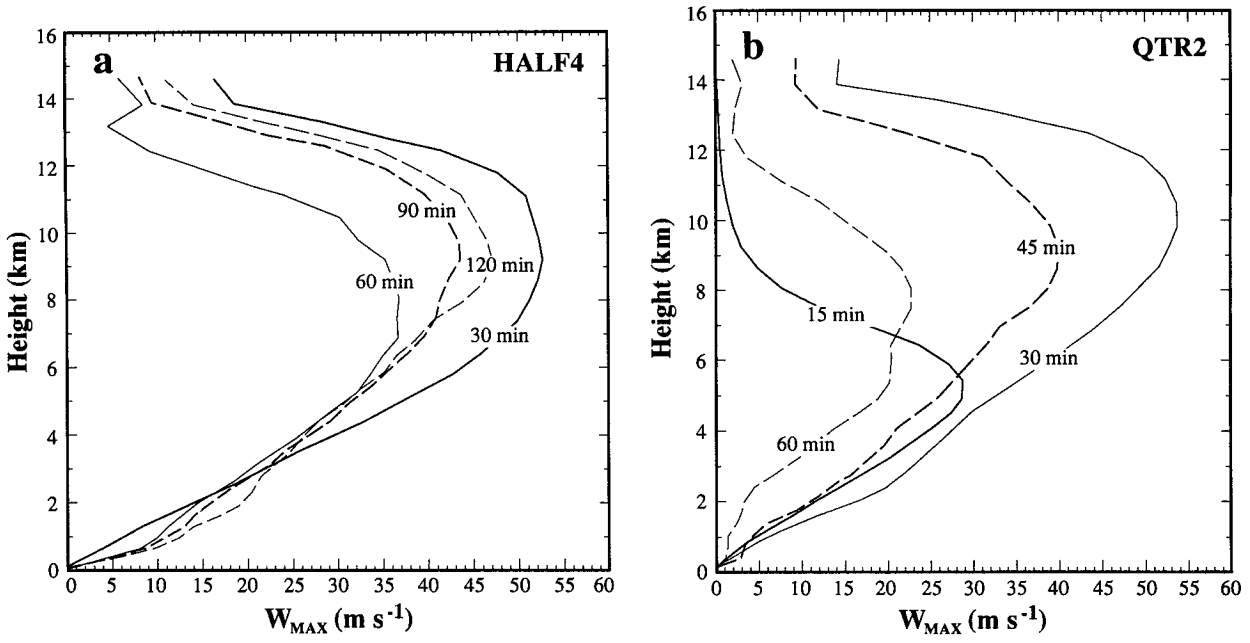

FIG. 5. Vertical profile of the maximum updraft (m s^{-1}) at selected times (min) for the initial storm in experiments (a) HALF4 (supercell) and (b) QTR2 (multicell).

at 60 and 90 min (Fig. 4a). This storm continues to move northeastward for a short period of time and then dissipates (also evident at a different altitude in Fig. 3f). The large values of vertical vorticity near z = 14 km in Fig. 6a are a result of environmental flow around the updraft's effluence, and although possibly exaggerated in intensity by their proximity to the upper boundary, appear to have little effect on overall storm structure or evolution.

In sharp contrast, the storm resulting from the initial disturbance in QTR2 exhibits markedly different structure and evolution, as shown in Figs. 4b, 5b, and 6b. The initial updraft intensifies rapidly (Figs. 5b and 2a) and produces a strong downdraft, associated with

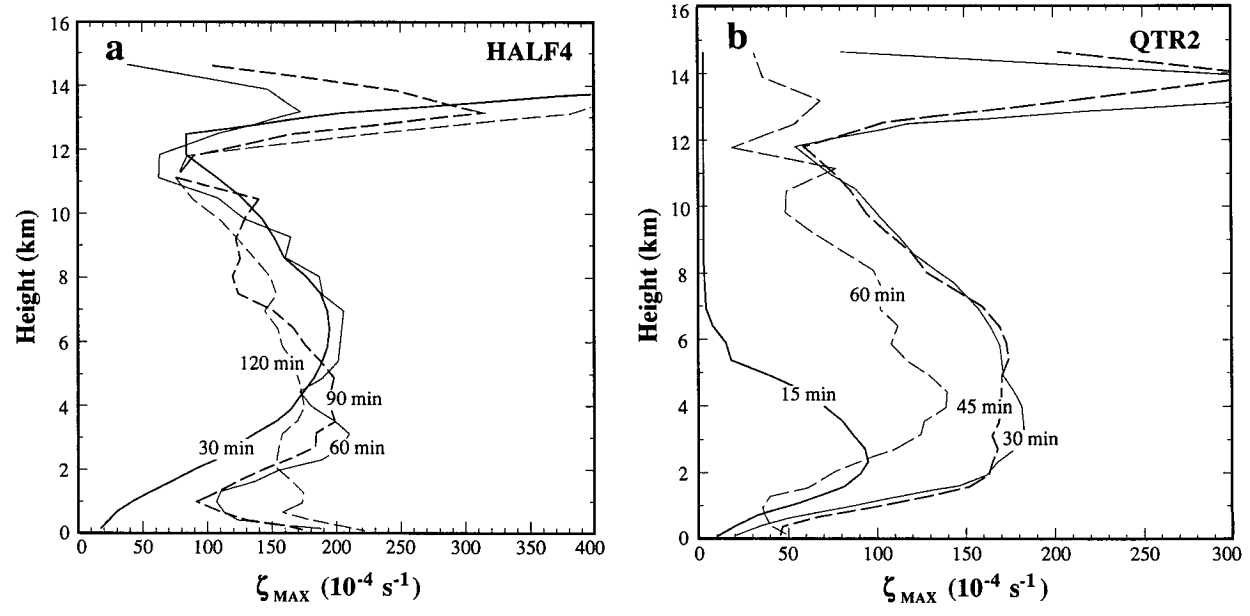

FIG. 6. As in Fig. 5 but for the maximum vertical vorticity (10^{-4} s^{-1}).

which is a surface cold pool (Fig. 4b) whose lateral propagation is largely unimpeded by the relatively weak (<5 m s^{-1}) low-level storm-relative winds. Because the incipient storm exhibits only modest lateral movement off the hodograph (Fig. 1), it is unable to keep up with the advancing gust front. Consequently, no mechanism exists for the generation of significant low-level rotation (Rotunno and Klemp 1985; Davies-Jones and Brooks 1993; Walko 1993) (Fig. 6b), though rather significant midlevel vorticity is evident during the mature phase of the storm.

The clear tendency for the model to produce distinctly different modes of convection in environments characterized by the same CAPE and identical shear magnitude but different shear profiles contradicts the conclusions of Rasmussen and Wilhelmson (1983) and Davies (1989). Therefore, *the mean shear cannot be a precise predictor of the rotational characteristics (or the tornadic potential) of convective storms.* One should consider, instead, the effects of other available data such as helicity, storm motion, and storm-relative inflow winds, as described in the following sections.

4. Comparison with linear theory

Despite the high degree of nonlinearity present in convective storms, considerable insight can be gained by applying linear theory to selected physical processes (e.g., storm propagation and rotation), because storm–environment interactions are described by linear terms such as $w(\partial\bar{\mathbf{V}}/\partial z)$. Indeed, linear terms, when comparable in magnitude to nonlinear terms, are important in nonlinear convection because they describe storm–environment interactions that bias certain properties such as the net rotation of an updraft (Rotunno and Klemp 1982).

In this section, we compare the actual correlation coefficients between w and ζ with those predicted by the Davies-Jones (1984) linear theory. We also show that this theory correctly predicts the relative positions of the temperature, vertical velocity, and vertical vorticity extrema during the early stages of storm development.

a. *Review of linear theory*

Using linear theory of dry, rotating, and inviscid convection, Davies-Jones (1984) showed that, during the initial stages of storm development, the correlation coefficient between w and ζ is given approximately by

$$r(w, \zeta) \approx Q\frac{\omega_s}{|\omega|}, \tag{5}$$

where ω_s is the environmental streamwise vorticity, $Q = (P^2 + 1)^{-1/2}$ is a penalty reduction factor that ranges from zero (maximum reduction) to unity (no reduction), and $P = \sigma D/|\bar{\mathbf{V}} - \mathbf{C}|$, where σ is the growth rate of the disturbance and D is a typical length scale for horizontal buoyancy gradients. The ratio $\omega_s/|\omega|$ in Eq. (5) may be written as

$$\frac{\omega_s}{|\omega|} = \frac{(\bar{\mathbf{V}} - \mathbf{C})\cdot\omega}{|\bar{\mathbf{V}} - \mathbf{C}|\,|\omega|} \equiv \text{NHD}, \tag{6}$$

where NHD is the *normalized helicity density* of the environment or, alternatively, the cosine of the angle between the environmental vorticity and storm-relative wind vectors. (Although *normalized helicity density* is also referred to as *relative helicity,* we prefer the former name to avoid the awkward and confusing expression "storm-relative relative helicity," and to conform with the standard terminology of the fluid dynamics community.) Clearly, |NHD| represents an upper bound for $|r(w, \zeta)|$. However, even when the low-level environmental vorticity is almost purely streamwise, an updraft may exhibit little overall rotation if the storm-relative winds are weak; that is, $Q \approx 0$.

In the shear layer of each of our experiments, the environmental streamwise vorticity varies directly with the NHD because $|\omega|$ is invariant there. Due to the curved shape of our hodographs, the NHD values are relatively large (see the following discussion). Consequently, if the implications of linear theory carry over to mature convection, then storms exhibiting only weak rotation should be associated with weak storm-relative winds.

The factor P defined above can also be viewed as the ratio of an advective time scale, $D/|\bar{\mathbf{V}} - \mathbf{C}|$ (based upon the time it takes an air parcel, moving with the storm-relative winds, to traverse a distance of about one updraft radius D), to a convective time scale, $1/\sigma$ (the convective e-folding growth time). When this ratio is large, the effects of the environmental winds on convection are small. The linear growth time is difficult to evaluate from atmospheric observations and is not applicable to storms initiated with a finite-amplitude disturbance in numerical models. Another problem is that σ is only relevant to the initial, exponential growth during a storm's life cycle. Thus, it is useful to recast $r(w, \zeta)$ into a form that 1) can be evaluated from a sounding and observed storm motion and that 2) might retain some predictive capability for nonlinear convection. Davies-Jones et al. (1984) accomplished this by replacing $1/\sigma$ with an equivalent time scale proportional to $H/(\text{CAPE})^{1/2}$, where H is the depth of the convection. Thus, P was substituted in their study by

$$P^* = \frac{(0.03\text{CAPE})^{1/2}}{|\bar{\mathbf{V}} - \mathbf{C}|}, \tag{7}$$

where the constant 0.03 was chosen such that $Q = 0.5$ when $|\bar{\mathbf{V}} - \mathbf{C}| = (\text{CAPE})^{1/2}/10$. Henceforth, $r(w, \zeta)$ will denote the theoretical correlation coefficient computed using P^* instead of P. This formula was used by Vasiloff et al. (1986) to show that changes in storm

motion were linked to the transformation of a multicell into a weak-evolution supercell storm.

In Figs. 7a and 7b we plot against $r(w, \zeta)$ and the NHD, respectively, the peak value (in time) of the *actual* correlation coefficient, $\rho(w, \zeta)_{max}$, for the initial storm in each simulation, where

$$\rho(w, \zeta) = \frac{\langle w\zeta \rangle}{(\langle w^2 \rangle \langle \zeta^2 \rangle)^{1/2}}, \quad (8)$$

and where $\langle \ \rangle$ denotes a horizontal average. We apply Eq. (8) only to those regions where $w > 1$ m s^{-1} using a horizontally windowed domain centered on the initial storm. Further, we vertically average both $r(w, \zeta)$ and NHD over the lowest 3 km (roughly the depth of the storm inflow) for the 0–4- and 0–8-km experiments, and only over the lowest 2 km for the 0–2-km experiments (because the quantities are indeterminate above the shear layer), in all cases using the storm motion defined previously. Because $\rho(w, \zeta)$ is a property of the updraft rather than of the environmental inflow, we average it over the layer 0–8 km to capture most of the rotational structure as well as the maximum updraft of the storm.

b. *Application to the simulated storms*

Figure 7a indicates that even the multicell updrafts rotate at some point in their life cycle (usually quite early as a result of the tilting of streamwise vorticity and midlevel vortex stretching) and that linear theory is apparently a good predictor of net updraft rotation, at least for this limited set of experiments. However, $r(w, \zeta)$ underestimates $\rho(w, \zeta)_{max}$ for all of the multicells and overestimates it slightly for all of the supercells (Fig. 7a). Nevertheless, $r(w, \zeta)$ provides a fairly clear-cut stratification of storm type: $r(w, \zeta) \leq 0.75$ for multicells and $r(w, \zeta) > 0.75$ for supercells, suggesting that the threshold value of 0.5 for mesocyclones proposed by Davies-Jones et al. (1984) may be somewhat low. As demonstrated in sections 5 and 6 (see also the Appendix), the SREH is the preferred parameter for operational use because of its computational stability and other attributes (Davies-Jones et al. 1990).

In sharp contrast to $r(w, \zeta)$, NHD shows no significant ability to predict $\rho(w, \zeta)_{max}$ (Fig. 7b) because it considers only the angle between the vorticity and storm-relative velocity vectors and neglects their magnitudes. Note that it considerably overestimates $\rho(w, \zeta)_{max}$ for all of the storms (Fig. 7b).

To better understand how the w–ζ correlations evolve, Fig. 8 shows time series of $\rho(w, \zeta)$ for the initial storm in all simulations. Focusing first on two representative cases, HALF4 (supercell, Fig. 8a) and QTR2 (multicell, Fig. 8b), we find that during the first 20–30 min both initial storms show similar rates of increase in $\rho(w, \zeta)$ as their motion deviates farther and farther off the hodograph. The supercell attains a higher peak in $\rho(w, \zeta)$, followed by a nearly constant value, while the peak in QTR2 is followed by a rapid decline associated with the demise of the initial storm. Rotation in subsequent updrafts of QTR2 (and those of other multicell experiments) reintensifies briefly as new but weaker updrafts form along the rapidly expanding gust front. In contrast, the supercell in HALF4, as well as those in the other supercell simulations, sustains its rotation for 60–90 min at a nearly constant value (Fig. 8).

Peak values of $\rho(w, \zeta)$ in Fig. 8 for the initial storms exceed 0.70 for all supercells, and range from 0.46 to 0.78 for all multicells. Thus, an important distinguish-

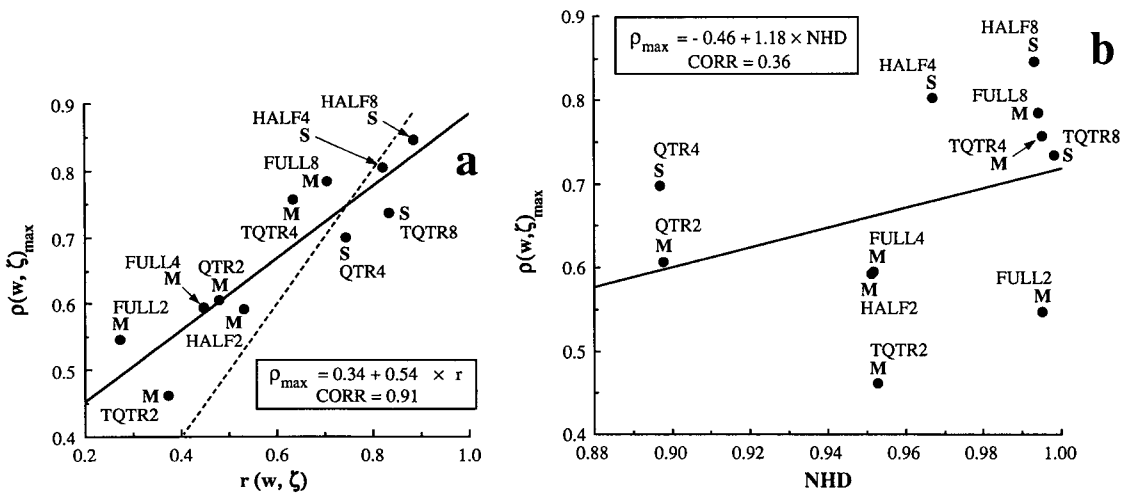

FIG. 7. Scatterplot of the maximum value (over time) of the correlation coefficient between vertical velocity and vertical vorticity averaged over the layer 0–8 km, $\rho(w, \zeta)_{max}$, as a function of (a) the theoretical correlation coefficient $r(w, \zeta)$ and (b) the normalized helicity density NHD, for all simulations. Also shown are the regression line, associated equation, and correlation coefficient: the dashed line in (a) defines $\rho(w, \zeta)_{max} = r(w, \zeta)$.

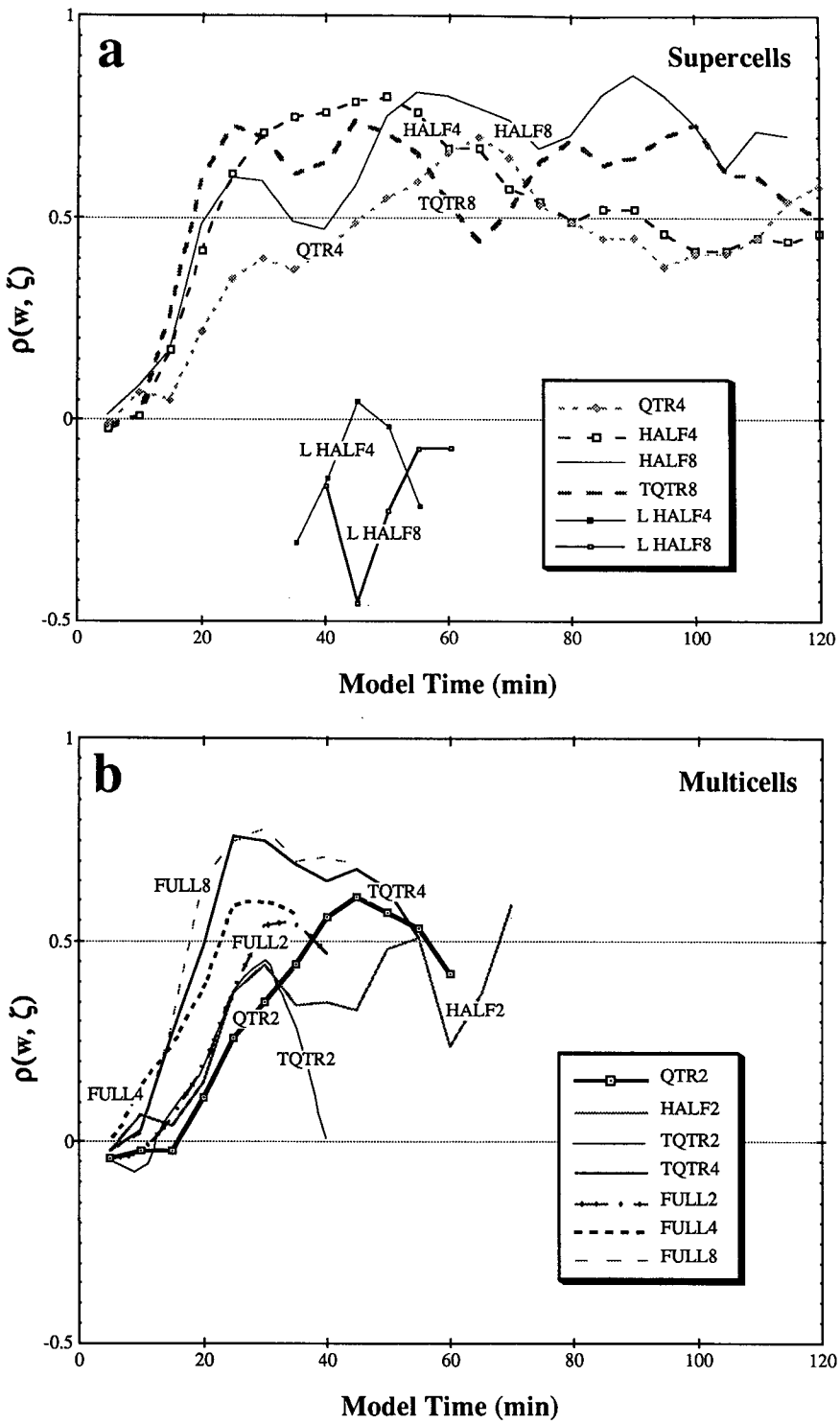

FIG. 8. Time series of the correlation coefficient between vertical velocity and vertical vorticity in the 0–8.0-km layer of the initial storm, $\rho(w, \zeta)$, for (a) all supercell experiments, showing also the left-flank storms in HALF4 and HALF8 (lower portion of figure) and (b) all multicell experiments.

ing characteristic between supercells and multicells in this set of simulations is not just the degree of correlation between the updraft and vertical vorticity per se (WK84, p. 2497) but also the time interval over which this correlation is sustained, nominally an hour or so for supercells. As a consequence, supercells also have the largest values of $\rho(w, \zeta)$ averaged in time (from 20 min to storm dissipation or the end of the integration), though one must be careful when interpreting this measure of rotation due to biases introduced by the relatively short lifetimes of the simulated multicells. With the exception of FULL8, the multicell storms, compared to the supercells, have smaller maximum values of vertical vorticity both at midlevels (between 1.14 and 8.0 km) and near the surface (below 1.14 km), with the midlevel maximum exceeding the near-surface one. Time series of vertical vorticity (not shown) generally indicate larger values at low levels and sustained, larger values at midlevels associated with the modeled supercells, in agreement with Fig. 9 of WK84. In all of our supercells except for HALF4, the maximum vertical vorticity is located at the lowest model level (127 m).

To demonstrate how the correlation between w and ζ develops in time and space, Fig. 9 shows, at 5-min intervals for experiment HALF4, single-valued contours of w, ζ, and the perturbation potential temperature θ' at $z = 3$ km, along with the orientation of the shear $\mathbf{S}$, vorticity ω, and storm-relative wind $(\mathbf{V} - \mathbf{C})$ vectors at $z = 2$ km. [Note that θ' is analogous to the vertical displacement field in Davies-Jones (1984).] The environmental vectors are shown for $z = 2$ km, rather than $z = 3$ km, to account for finite vertical displacements of air parcels. Data show (e.g., Davies-Jones and Henderson 1975; Fig. 2 of Johnson and Brandes 1986) that the horizontal momentum of air rising in updrafts is partly conserved, so that the wind direction in updrafts tends to match that in the environment at a lower level.

In agreement with linear theory, after allowing for vertical advection, the tilting of horizontal vorticity into the vertical by the initially axisymmetric thermal disturbance produces a vortex couplet centered on the updraft and aligned with the storm-relative wind vector, resulting in a nearly zero net correlation between ζ and θ' (Figs. 9a,b). Also, as predicted by linear theory, the peak updraft is displaced to the (storm-relative) upwind side of the θ' field (compare with Figs. 5, 7, and 8 of Davies-Jones 1984). After about 10 min, the disturbance slows down and begins to move toward the north-northwest instead of the northwest as it grows in vertical extent. As a result, the vorticity and storm-relative wind vectors at $z = 2$ km become increasingly aligned (Figs. 9c–f) (i.e., the vorticity is becoming highly streamwise), leading to an increase in the correlation between w and ζ. These two fields become even more correlated as the nonlinear effect of vortex stretching intensifies vorticity in convergent regions until, by 30 min, the centers of updraft, cyclonic vorticity, and buoyancy are nearly coincident (but still in the relative positions predicted by linear theory).

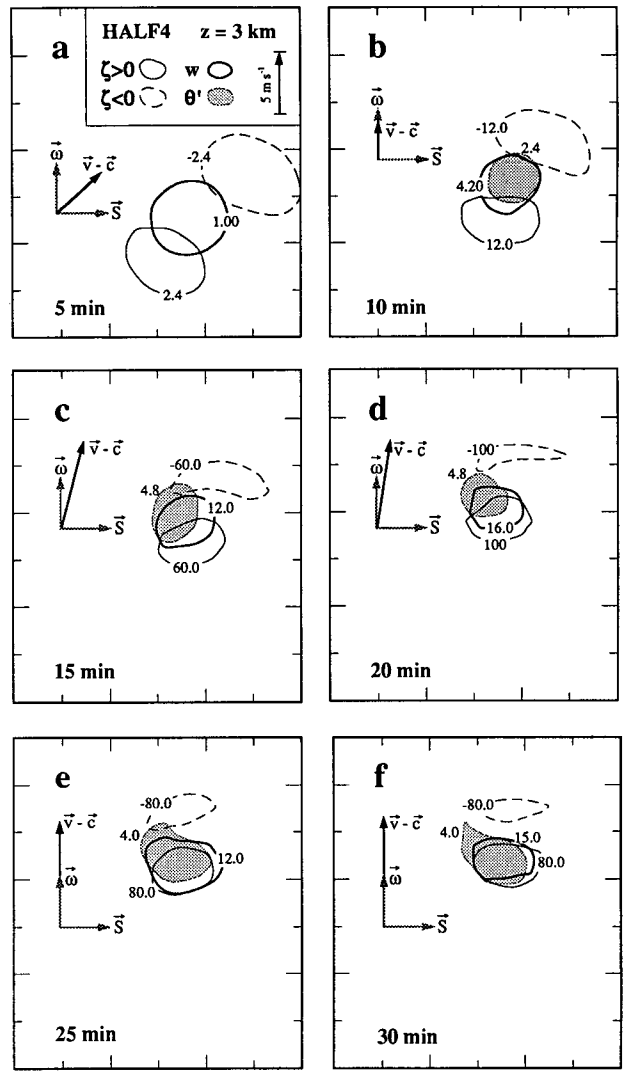

FIG. 9. Single-value contours (values as indicated), at an altitude of 3 km, of updraft w (m s^{-1}, bold solid line), positive (thin solid lines) and negative (dashed lines) vertical vorticity ζ (10^{-4} s^{-1}), and perturbation potential temperature θ' (K, stippled) at 5-min intervals for simulation HALF4. Only a windowed portion of the total domain is shown, and tick marks are spaced 3 km apart. The inset in each panel depicts the ambient wind shear vector $\mathbf{S}$, vorticity vector ω, and storm-relative wind vector $(\mathbf{V} - \mathbf{C})$ at $z = 2$ km. The θ' contour is missing from panel (a) because the thermal disturbance is still below 3 km at 5 min.

5. Storm motion effects

Storm motion is known to be linked to the development and maintenance of rotation in deep convection. As described in sections 1 and 4, Davies-Jones (1984) and others have shown that environmental

streamwise vorticity is associated with the onset of updraft rotation in supercells, with the strength of the low-level storm-relative winds serving as a principal controlling influence. In particular, if the environmental winds are weak compared to those induced by the storm, then the former have little effect on storm structure. We examine in this section the validity of these and related issues for our simulations.

Table 4 shows the SREH for the model initial environments based on the motion of the initial storm (bold numbers) and on the 0–12-km density-weighted mean winds. Although these values are obtained from the discretized soundings, they agree to within 1% of those computed analytically as described in the Appendix.

Focusing first on actual storm motions, a comparison with storm types suggests an SREH threshold for supercells of approximately 250 $m^2 s^{-2}$ rather than the 157 $m^2 s^{-2}$ proposed for mesocyclones by Davies-Jones et al. (1990). This upward revision is due mostly to experiment FULL8, which—though classified as a multicell with a SREH of 205 $m^2 s^{-2}$—produces substantial vertical vorticity for brief periods of time. Due to the circular hodograph, storms in FULL8 show little ground-relative movement and thus never encounter storm-relative inflows greater than about 6 m s^{-1}. Consequently, the inflows are insufficiently strong to prevent the cold pool from surging well ahead of the updrafts.

Because the SREH depends upon the scalar product of the vorticity and storm-relative wind vectors, weak (strong) winds coupled with large (small) streamwise vorticities can yield identical values of SREH. In experiment FULL8, it is primarily the low-level turning and not the magnitude of the storm-relative winds that contributes to the large SREH. To illustrate the importance of these two parameters for all simulations, Table 5 shows the storm-relative turning angle and mean storm-relative wind speed over the 0–3-km layer computed using the motion of the initial storm and the *initial* (i.e., base-state) ground-relative environmental winds. (Although the mean flow and thus the mean hodograph change with time, it is appropriate to base the turning angle and storm-relative wind calculations on the *initial* hodograph because the mean depends arbitrarily upon the averaging volume, and because the initial low-level winds, unlike the mean winds, are not contaminated by the surface cold pool.)

TABLE 4. Storm-relative environmental helicity $\mathscr{H}_v$ ($m^2 s^2$) over the layer 0–3 km for the initial storm in each simulation (shown in bold numbers). Storm motion was computed by tracking the updraft maximum at z = 3 km from 20 min until its demise, disappearance from z = 3 km, or termination of the simulation. Also shown is $\mathscr{H}_v$ computed using the 0–12-km density-weighted mean wind. Storm type is indicated by M for multicell and S for supercell.

	Shear layer (km)		
Hodograph shape	0–2	0–4	0–8
Quarter circle (QTR)	**80** 50 (M)	**287** 154 (S)	N/A
Half circle (HALF)	**91** 71 (M)	**321** 219 (S)	**402** 378 (S)
Three-quarter circle (TQTR)	**57** 59 (M)	**169** 191 (M)	**311** 316 (S)
Full circle (FULL)	**39** 39 (M)	**106** 131 (M)	**205** 203 (M)

TABLE 5. Turning angle (°) between the storm-relative environmental wind vectors at 0- and 3-km altitude, and the magnitude of the storm-relative environmental wind speed (m s^{-1}) averaged over the layer 0–3, using the storm motion as defined for Table 4. Positive turning angles imply clockwise rotation of the storm-relative wind vector. Storm type is indicated by M for multicell and S for supercell.

Experiment (storm type)	Turning angle (°)	$\lvert \mathbf{V} - \mathbf{C} \rvert$
QTR2 (M)	152	3.0
HALF2 (M)	149	3.4
TQTR2 (M)	246	1.1
FULL2 (M)	360	0.8
QTR4 (S)	94	12.7
HALF4 (S)	93	12.7
TQTR4 (M)	187	4.6
FULL4 (M)	294	0.7
QTR8	N/A	N/A
HALF8 (S)	78	15.9
TQTR8 (S)	102	11.6
FULL8 (M)	153	6.2

In each of the four supercell simulations, the 0–3-km average storm-relative wind speed is greater than 10 m s^{-1} and the turning angle is 75° or greater; the multicell storms generally show lower speed values but larger turning angles, corroborating the results of Davies-Jones (1984). Apparently, no amount of turning can compensate for the absence of sufficient low-level, storm-relative flow in simulations such as TQTR2 and FULL4, thereby resulting in nonsupercell storms despite hodographs possessing substantial curvature. Note that the mean storm-relative inflow wind speeds show a monotonic increase as the storm type changes from multicell to supercell, with the "near miss" case (FULL8) intermediate between the other multicells and the supercells. These results suggest that storm-relative inflow of at least 10 m s^{-1} in the 0–3-km layer is a *necessary condition* for supercell storms, and that the turning of the storm-relative winds with height is somewhat less important provided that the angle subtended by the storm-relative wind vectors between 0 and 3 km is sufficient to yield large helicity.

It is important to recognize that the SREH can change markedly during the lifetime of a storm as a result of changes in storm motion. Figure 10 shows, for experiment HALF4, how the storm motion vector, based on tracking the updraft maximum at z = 3 km over successive 30-min time windows, changes with time relative to the base-state hodograph. Superposed on this figure are contours of SREH as a function of storm motion (Davies-Jones et al. 1990). During the first half hour of the simulation, the initiating distur-

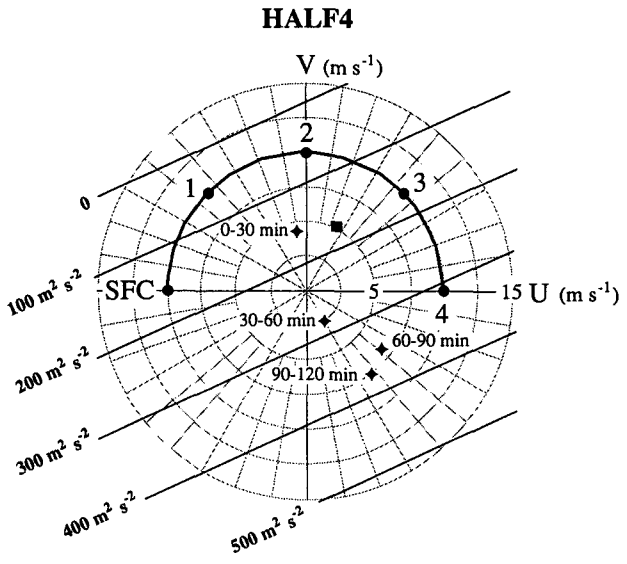

FIG. 10. Wind hodograph for simulation HALF4. The solid square is the density-weighted mean wind in the layer 0–6 km, and the stars represent the motion of the initial storm, based on tracking the updraft maximum at $z = 3$ km, over the periods shown. Concentric circles are separated by 2.5 m s^{-1}, and hodograph labels are altitude (km). Also shown are contours of the storm-relative environmental helicity (parallel thin solid lines) computed following Davies-Jones et al. (1990).

bance moves in the general direction of the low-level flow at roughly half the speed of the winds at $z = 1.75$ km; thus, the motion vector lies well within the semicircle defined by the hodograph. Once the rain-induced cold pool is established at approximately 30 min, the initial storm becomes an extreme right mover, propagating toward the southeast along the expanding gust front (Fig. 4a) such that its motion vector actually lies *outside* of the semicircle. This transition in storm movement has two important consequences. First, it is associated with a dramatic increase in the 0–3-km storm-relative winds (from 5 m s^{-1} between 0 and 30 min to over 15 m s^{-1} between 30 and 60 min), and second, it increases substantially the SREH. Fujita (1965) associated sharp right turns in storm motion with the onset of rotation, and the resumption of a normal course with the cessation of rotation.

To determine whether these changes invoke similar noticeable alterations in storm structure, Fig. 11 shows, for experiment HALF4, relationships among the ground-relative position of the updraft maximum at $z = 3$ km, the surface gust front location, and the SREH as a function of time. The latter is computed using the *average motion of the initial storm over the four 30-min periods shown,* and is shown by the bold numbers centered on the averaging times. Shown in the inset table are the maximum updraft and w–ζ correlation coefficient $\rho(w, \zeta)$ associated with the initial storm. As the storm changes direction at approximately 30 min, the SREH nearly doubles from 151 m^2 s^{-2} at 15 min to 273 m^2 s^{-2} by 45 min, during which $\rho(w, \zeta)$ increases markedly in association with mesocyclone development. Although the helicity values are well above the threshold for mesocyclones ($\sim$250 m^2 s^{-2}), and a mesocyclone is present from 30 min onward, minor variations in helicity do not correlate with minor changes in either $\rho(w, \zeta)$ or maximum vertical vorticity. However, it would be naive to expect that changes in mesocyclone intensity are governed solely by changes in storm motion, the latter being all that linear theory can consider.

6. Predictors of storm characteristics

From a practical forecasting standpoint, it would be advantageous to condense the large dimensional parameter space that defines the storm environment (or equivalently, defines model inputs, e.g., base-state sounding) into a *single parameter* that predicts storm characteristics (or equivalently, model outputs, e.g., storm type, motion, rotational characteristics). We believe this to be an unlikely or perhaps impossible task for a number of reasons. First, storm-scale models have recently been shown to exhibit extreme sensitivity to initial conditions in some cases (McPherson 1991; McPherson and Droegemeier 1991; Brooks 1992), though the degree to which this behavior is a function of input parameters (e.g., base-state wind and thermodynamic structure, boundary conditions) is cur-

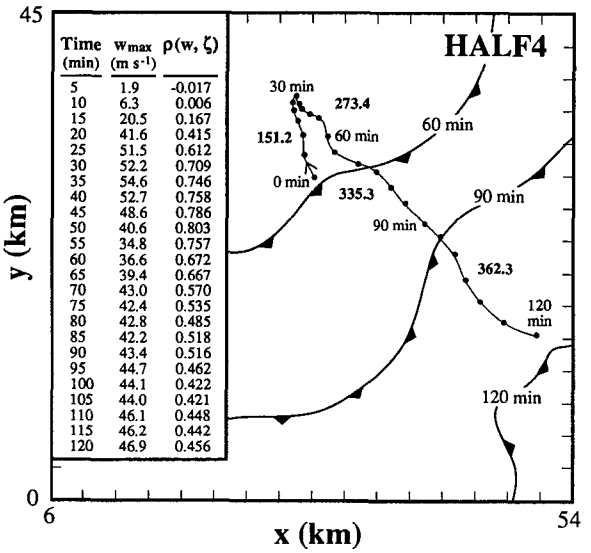

Time (min)	Wmax (m s-1)	ρ(w, ζ)
5	1.9	-0.017
10	6.3	0.006
15	20.5	0.167
20	41.6	0.415
25	51.5	0.612
30	52.2	0.709
35	54.6	0.746
40	52.7	0.758
45	48.6	0.786
50	40.6	0.803
55	34.8	0.757
60	36.6	0.672
65	39.4	0.667
70	43.0	0.570
75	42.4	0.535
80	42.8	0.485
85	42.2	0.518
90	43.4	0.516
95	44.7	0.462
100	44.1	0.422
105	44.0	0.421
110	46.1	0.448
115	46.2	0.442
120	46.9	0.456

FIG. 11. Locations of the updraft centroid at $z = 3$ km in ground-relative coordinates, shown every 5 min for the initial storm in experiment HALF4. The gust front location is shown at 30-min intervals by the thin barbed lines, and bold numbers along the storm track are the storm-relative environmental helicity $\mathscr{H}_v$ over the layer 0–3 km (m^2 s^{-2}) computed at 15, 45, 75, and 105 min using 30-min average storm motions centered at these times. Tick marks are shown at 3-km intervals, and the inset table shows the w–ζ correlation coefficient and maximum updraft associated with the initial storm at 5-min intervals. The former is computed as a vertical average over the layer 0–8 km.

rently under investigation. Further, as shown above, storm motions vary both temporally and between neighboring storms, and are influenced strongly by boundary-layer convergence lines.

With these limitations in mind, we examine in this section the utility of several parameters in predicting the characteristics of our modeled storms (e.g., storm type, intensity of low- and midlevel rotation). In contrast to the BRN, which uses the CAPE and environmental shear to characterize model input by a single number, the SREH parameterizes the input as a *function of storm motion,* which—though an output of the model—is in practice an observable quantity readily available to the forecaster (Davies-Jones et al. 1990). This leads to different predictions for storms with different mean motions. It is important to note that the 0–2-km mean shear magnitude used as a predictor by Davies (1989), which is identical in all our simulations, is above the threshold for tornadic mesocyclones. Consequently, by that measure alone, each of our simulations should produce supercell storms.

a. 0–3-km SREH and BRN shear

Figures 12a and 12b show, during the lifetime of the initial storm in each simulation, the maximum vertical vorticity above and below 1.14 km, respectively (the level we chose to distinguish between mid- and low-level rotation), as a function of the SREH. Care has been taken to ensure that the low-level (below 1.14 km) vorticity is that associated with the storm updraft, and not with shear along the gust front. Interestingly, the four (seven) simulations exhibiting supercell (multicell) characteristics are generally at the upper (lower) ends of both the vorticity and SREH scales. One storm, FULL8, has an intermediate SREH with maximum vertical vorticities similar to those of the four supercells. The threshold for supercells appears to lie near $\mathscr{H}_v \approx 250$ m^2 s^{-2}, which again is considerably larger than the value given by Davies-Jones et al. (1990). This disagreement is perhaps due to the sometimes relatively poor sampling of the immediate storm environment by proximity soundings, which were used in their study, to the rather small number of simulations composing the present parameter space, or to differences between the real atmosphere and the numerical model.

Figures 13a,b present the same information as in Fig. 12, though with respect to the BRN shear (or equivalently for BRN^{-1} since the base-state CAPE is the same in each of our simulations). These results agree quite favorably with the overlapping regions for supercell and multicell storms proposed by WK82 and WK86. Surprisingly, the BRN shear is a *better* predictor of maximum vertical vorticity than the SREH.

It is important to recognize that, by itself, *the vertical vorticity implies nothing about net updraft rotation.* For example, the initial storms in the WK82 and Rotunno and Klemp (1985) unidirectional-shear simulations split near 40 min (except for the $U_s = 15$ m s^{-1} case in WK82), when vertical vorticities close to mesocyclone intensity are already present. However, because these vortices are at midlevels and are located symmetrically on the flanks of the initial updraft, they pose little practical threat (i.e., they are not typically considered to be mesocyclones) and result in near-zero net updraft rotation. It is not until the initial storm splits, and the resulting storms evolve into right- and left-moving supercells, that the updrafts acquire net rotation. Because the BRN is the same for each storm in a given simulation, independent of storm motion, it fails to predict either the magnitude or the sense of net updraft rotation. For the curved hodographs used here, we find that the SREH is clearly superior to the BRN in predicting net updraft rotation, as measured by $\rho(w, \zeta)_{\max}$, largely because it considers the storm-relative winds and associated streamwise vorticity (Figs. 14a,b).

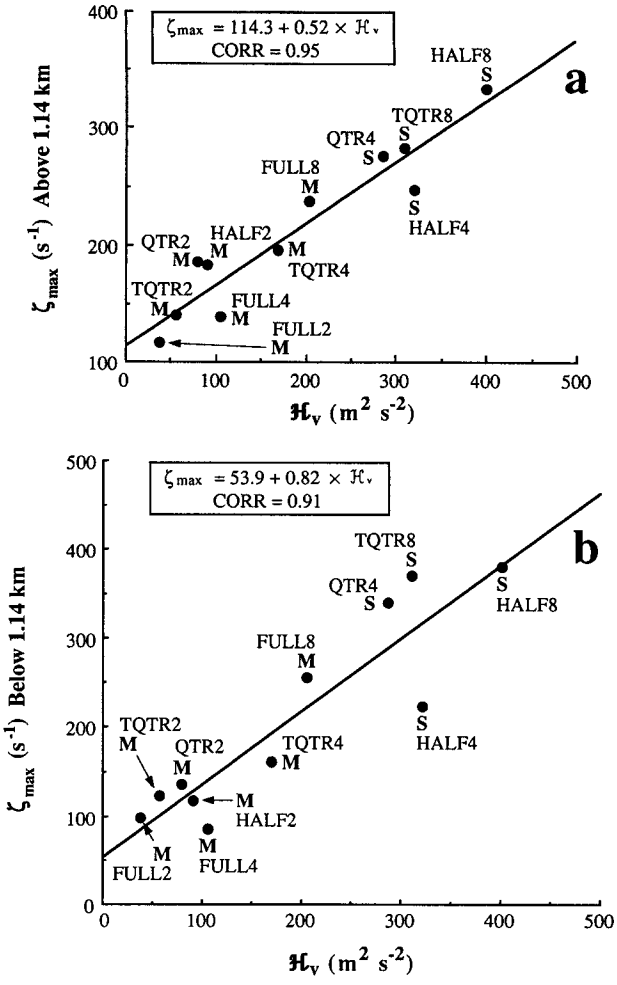

FIG. 12. As in Fig. 7 but for the maximum vertical vorticity associated with the initial storm (a) above and (b) below $z = 1.14$ km, plotted against the storm-relative environmental helicity.

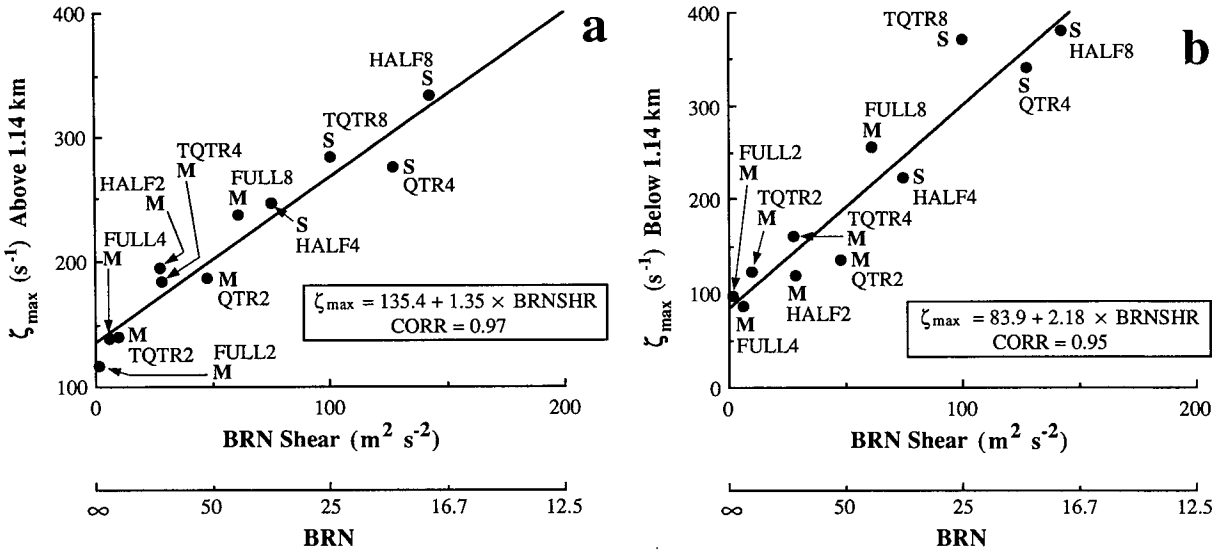

FIG. 13. As in Fig. 12 but plotted against the bulk Richardson number (BRN) and BRN shear [denominator in Eq. (2)].

Large values of low-level vorticity develop slowly in our simulations and in those of WK84, and await storm splitting in the unidirectional-shear cases of WK82. Rotation near the ground is believed to be derived principally from baroclinically generated horizontal vorticity rather than environmental vorticity. Therefore, the high correlations shown here between maximum vertical vorticity and the BRN shear (and other parameters as well) are surprising.

The "influence of helicity" referred to in the title of this paper can, in light of the foregoing, be clearly demonstrated by returning to the time series of $\rho(w, \zeta)$, including the left-flank storms in experiments HALF4 and HALF8 (Fig. 8a). Although the BRN is the same for the right- and left-flank storms in a given experiment, the behavior of these storms is clearly quite different. Both left movers lie on the concave side of their respective hodographs but exhibit weaker storm-relative flow than their right-moving counterparts (Fig. 1). Thus, according to linear theory, they should also exhibit smaller $w-\zeta$ correlations, as verified by the model results. In these cases, as in WK84, the $w-\zeta$ correlations in the left-flank storms are slightly negative even though the SREH is positive. This result does not contradict linear theory because the inflow to the left mover is affected by the presence of the much larger right-mov-

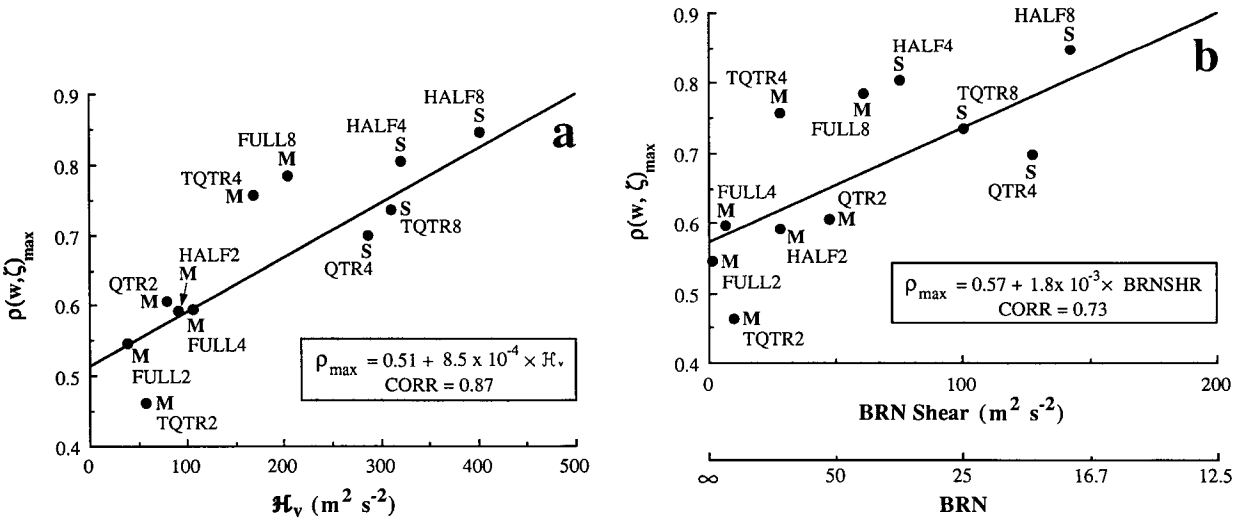

FIG. 14. As in Fig. 7 but plotted against (a) the storm-relative environmental helicity associated with the initial storm and (b) the bulk Richardson number (BRN) and BRN shear.

ing storm; that is, the left mover evolves in a vertical shear profile that differs substantially from that of the distant environment or base state. The right-moving storms generally show sustained w–ζ correlations on the order of 0.6 to 0.7, in agreement with the curved-hodograph simulations of WK84 (see their Fig. 10). Comparisons with time series of maximum vertical vorticity (not shown) demonstrate, as one would expect, that ζ grows more rapidly in time than $\rho(w, \zeta)$ because the storm motion vector is initially near the hodograph. The behavior of the multicells (Fig. 8b) is generally as described earlier, with rapid development of updraft rotation followed relatively quickly by storm demise.

b. Other parameters

Table 6 shows, for all experiments, linear correlation coefficients between a number of parameters that characterize the ambient environment and those that provide some measure of vertical rotation, including those discussed in Fig. 7 and Figs. 12–14. The worst predictor of rotational properties is clearly the NHD, and the best are those that explicitly account for the strength of the low-level storm-relative winds, including parameters as basic as $|\mathbf{V} - \mathbf{C}|$. Overall, the SREH and $r(w, \zeta)$ show the greatest degree of consistency and skill in predicting the sense and magnitude of both overall updraft rotation [i.e., $\rho(w, \zeta)_{\max}$] and the maximum vertical vorticity itself. The parameters that provide a clear threshold for storm type are the BRN shear, $r(w, \zeta)$, $\mathscr{H}_v$, $|\mathbf{V} - \mathbf{C}|$, and Q. Of these, the BRN shear is preferred because it is independent of storm motion.

TABLE 6. Correlation coefficients between the parameters shown in the left vertical column and the maximum w–ζ correlation coefficient averaged from the surface to 8 km [$\rho(w, \zeta)_{\max}$], the maximum vertical vorticity between 1.14 and 8 km ($\zeta_{\max}$), and the maximum vertical vorticity between the surface and 1.14 km (ζ_{sfc}) associated with the initial storm in all simulations.

Environmental parameter	$\rho(w, \zeta)_{\max}$	$\zeta_{\max}$	ζ_{sfc}
NHD (0–2- or 0–3-km average)[a,b]	0.36	0.11	0.16
ω_s (0–3-km average)[b]	0.82	0.63	0.62
$r(w, \zeta)$ (0–2- or 0–3-km average)[a,b]	0.91	0.96	0.88
BRN shear [denominator of Eq. (2)]	0.73	0.97	0.95
$\mathscr{H}_v$ [0–3 km, as in Eq. (4)][b]	0.87	0.95	0.91
$\mathscr{H}_v$ (0–3 km, computed using the 0–12-km density-weighted mean winds)	0.85	0.87	0.84
$\lvert\mathbf{V} - \mathbf{C}\rvert$ (0–3-km average)[b]	0.81	0.96	0.92
$r(w, \zeta)$/NHD[c]	0.88	0.96	0.88

[a] A 2-km averaging interval is used only when the base-state shear does not extend above 2 km.

[b] Based on the motion of the updraft maximum at $z = 3$ km for the initial storm from 20 min until its demise at 3 km.

[c] An effective penalty factor Q [see Eq. (5)].

c. Discussion

We have demonstrated in this section that the magnitude of the storm-relative wind is a key factor in predicting storm type and rotational properties, and that $r(w, \zeta)$ and the SREH exhibit a strong potential for operational use, despite their dependence upon a parameter (storm motion) that is not estimable with high accuracy from the prestorm environment but can be readily obtained from conventional radar data. Although the BRN certainly shows skill in predicting storm type—as demonstrated by WK82 and WK84, along with the maximum vertical vorticity, as shown above—it can neither distinguish among storms forming in the same general environment (e.g., the left and right movers of a split pair) nor provide reliable information regarding net updraft rotation. The reasons for this, in comparison to the SREH, are clear: large values of SREH are predicated on strong low-level streamwise vorticity (the ingredient for updraft rotation) and strong storm-relative winds (which prevent the surface cold pool from spreading out ahead of the storm and blocking the supply of unstable air to the updraft). *Thus, from an operational viewpoint, it seems prudent to use the BRN to predict storm type because it is independent of storm motion, and the SREH to characterize the rotational properties of storms once their motions can be established.*

As pointed out by one reviewer and discussed earlier, the SREH, unlike the BRN, is not a *pure* predictor of storm properties because it depends upon an output of the model (storm motion). Thus, comparisons between the BRN and SREH are somewhat unfair. To address this issue, we examined another parameter, the mean-wind helicity, which is the helicity computed using an unbiased estimate of storm motion, namely, the 0–12-km density-weighted mean wind (see Table 4). The mean-wind helicity predicts net updraft rotation better than the BRN shear, but with less skill than the SREH (as expected). The former is due to the fact that, for the curved hodographs used here (Fig. 1), the mean wind lies on the concave side of the profile; further, the mean-wind-relative winds veer with height. Clearly, even crude estimates of storm motion will yield useful predictions of mesocyclone potential for such environments.

7. Characterizing flow stability and rotation

Fluid dynamicists have, for the past several years, employed the NHD to characterize the structure and stability of homogeneous turbulent flows (e.g., Pelz et al. 1985). Originally, it was believed that regions of low (high) NHD tend to be more (less) susceptible to dissipation (Moffatt 1985). Although subsequent studies by Pelz et al. (1986), Kerr (1987), Wallace and Balint (1990), and several others have cast serious doubt on this hypothesis, it is important to note, as

pointed out by Moffatt and Tsinober (1992), that the NHD is not Galilean invariant and thus should be computed in the reference frame of the locally dominant, large-scale structure. This is easily accomplished in models of isolated convective storms, but is much more arduous for homogeneous turbulence, thus making difficult a physically meaningful interpretation of NHD in the latter. The use of conditional sampling techniques (conditioned upon low dissipation) in some of the turbulence studies further complicates the issue (Moffatt and Tsinober 1992) because, although large NHD implies low dissipation, low dissipation does not necessarily imply large NHD (e.g., Tsinober 1990).

We therefore believe that the NHD should not yet be discounted as potentially useful in the context of convective storms. Indeed, Brandes et al. (1988) showed, for a rotating storm observed by Doppler radar, that the frequency distribution of the NHD was not symmetric about zero but exhibited a rather distinct peak near positive unity. Their results, along with the linear theory of Davies-Jones (1984), demonstrate that a disturbance growing in an environment with zero vertical helicity converts horizontal environmental helicity into (disturbance) vertical helicity, $\int w\zeta d\Omega$. A similar finding was obtained in a numerical simulation study by Wu et al. (1992).

To examine the behavior of the NHD in our simulations, we compute it for the disturbance flow (e.g., Lilly 1986b) associated with the initial storm. The values so obtained are then placed within 1 of 20 bins in a frequency distribution. Points at which the disturbance vorticity and velocity are close to zero and thus produce erroneous or indeterminate NHD, as in the undisturbed environment, are categorized separately. Although the averaging involved in obtaining the disturbance flow is a function of the chosen volume, we found the results to be qualitatively similar when various averaging volumes and thresholds used to define "very small" values of velocity and vorticity were used (Lazarus 1990).

Figure 15 shows histograms of the disturbance NHD for two representative experiments, HALF4 [supercell, panel (a)] and QTR2 [multicell, panel (b)]. In both cases, the mean disturbance NHD is indefinite at $t = 0$. If the disturbances in both experiments had no statistical preference for a given helicity value, one would expect the distributions to be flat (e.g., Pelz et al. 1985), that is, an equal probability for all bins, with each containing 0.05 of the volume fraction or $1/20$ of the total number of points. However, such is not the case. The disturbance NHD shows a clear bias toward large positive values in HALF4 (Fig. 15a), with monotonic growth in the 0.95 bin evident in time throughout the simulation. The number count in the indeterminate category (Ind.) decreases with time as the volume affected by the storm increases.

In contrast, multicell simulation QTR2 (Fig. 15b) shows a flatter distribution with less pronounced skewness of the disturbance NHD toward large positive values, principally because the associated storms are short-lived and the storm-relative winds are weak (generally 5 m s^{-1} or less over the 0–3-km layer). Note the clustering of values near zero after 15 min. Similar results are evident for the other multicell simulations, suggesting that this type of convection is inefficient in converting mean to disturbance normalized helicity density.

8. Summary and discussion

We used a three-dimensional numerical cloud model to examine the role of helicity in convective storm morphology, with an emphasis on understanding those factors responsible for producing long-lived, rotating

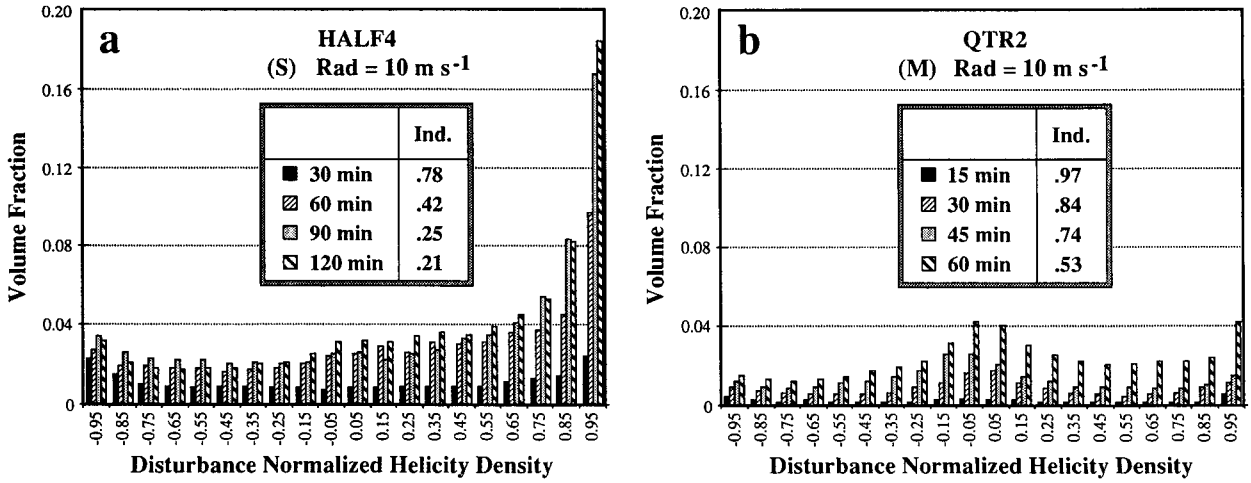

FIG. 15. Histograms of the disturbance normalized helicity density (NHD′) at 30-min intervals for experiments (a) HALF4 and (b) QTR2. Those points for which NHD′ is indeterminate (Ind.) are tabulated in the inset, and the radii of the hodographs (m s^{-1}) are as listed.

storms. Eleven simulations (an admittedly small sample) were conducted in which the depth of the ambient shear layer and the hodograph turning angle were systematically varied while holding constant the magnitude of the vertical shear in the shear layer. In this manner, the simulations covered a wide range of environmental helicities. Unidirectional or nearly unidirectional wind profiles were not considered.

In general, the types of storms produced by the model agreed with the bulk Richardson number (BRN) categorizations proposed by Weisman and Klemp (1982, 1984, 1986). However, we found that the storm-relative environmental helicity (SREH) and the theoretical correlation coefficient between vertical velocity and vertical vorticity were considerably better discriminators of net updraft rotation than the BRN, though the BRN showed slightly better skill in predicting the maximum vertical vorticity.

In contrast to results presented by Davies (1989), which suggest that the tornadic potential (and implicitly the rotational characteristics) of storms can be predicted by the 0–2-km mean shear, the present results show that the shear *profile* (and storm motion), not the mean shear itself, determines storm rotational characteristics. In our simulations, the supercell updrafts, in comparison to their multicell counterparts, developed more slowly and never quite reached the same maximum vertical velocity. They did, however, become quasi-steady at relatively large updraft intensities, instead of declining after 30 or so minutes. Although even the multicell updrafts rotated briefly, rotation in the supercell updrafts was much stronger and lasted for 90 min or longer.

We examined the SREH, computed over an inflow depth of 3 km, as an indicator of storm type and rotation potential, and considered separately the contributions made to this quantity by the storm-relative winds and hodograph turning angle in the 0–3-km layer. Although the threshold of the SREH for the modeled supercell storms (250 $m^2 s^{-2}$) was somewhat larger than that obtained for observed storms by Davies-Jones et al. (1990) (157 $m^2 s^{-2}$), we found the agreement encouraging.

The simulations also showed that storm-relative winds of at least 10 m s^{-1} in the 0–3-km layer appear necessary for obtaining supercells, and that the turning of the storm-relative wind vector in this layer is somewhat less important provided that the SREH is large. As the storm-relative winds weakened progressively below 10 m s^{-1}, even for hodographs possessing considerable curvature, multicells formed. During the storm growth phase, the relative locations of the temperature, vertical velocity, and vertical vorticity extrema agreed well with predictions made by linear theory after allowance for the effects of vertical advection.

By examining a number of parameters based on readily observed data and deemed plausible for characterizing storm rotational properties, those that included some measure of the magnitude of the storm-relative winds were found to perform the best, with the SREH and theoretical w–ζ correlation coefficient $r(w, \zeta)$ having the highest overall skill. The success of $r(w, \zeta)$ verifies that linear theory can be extended with some degree of success to the mature storm phase. The environmental normalized helicity density was found to be a very poor predictor of storm rotation due to its neglect of the magnitudes of the vorticity and storm-relative wind vectors. The BRN shear was found to be a slightly better predictor of maximum vertical vorticity than the aforementioned parameters, while the BRN shear, SREH, and $r(w, \zeta)$ showed good skill in determining storm type. Thus, from an operational viewpoint, we recommend using the BRN or BRN shear to predict storm type because they are independent of storm motion, and the SREH to characterize the rotational properties of storms once their motions can be established.

Finally, histograms of disturbance normalized helicity density were shown to have a distinct bias toward large positive values for supercells, while storms considered to be multicell in character exhibited a much weaker bias. Although we have not yet examined detailed helicity or energy budgets to determine objectively whether reduced dissipation is present in those storms characterized by large SREH, we do feel that our results clearly show helical storms to be longer-lived than their nonhelical counterparts, and the SREH to be a much better predictor of net updraft rotation than the BRN. The presumed absence of a clear connection between measures of helicity and dissipation in homogeneous turbulent flows should not discourage continued investigation of such linkages in isolated thunderstorms, particularly because the appropriate frame of reference for the latter is well defined. We therefore continue to pursue this problem using improved simulation models, particularly with respect to the treatment of subgrid-scale processes and more complete analysis methods.

The degree to which helical storms, by virtue of their extended lifetimes and dynamical stability, are more predictable than other types of convection remains to be shown. McPherson (1991), McPherson and Droegemeier (1991), and Brooks (1992) have demonstrated that the evolution of a simulated helical supercell storm can, in some instances, be altered significantly by relatively minor changes to the initiating thermal disturbance. On the other hand, there may be critical times in the lifetime of a supercell storm where only slight differences in *current* storm structure lead to radically different evolutions (R. McPherson, personal communication). Such times may occur when storms are on the verge of splitting or of making a transition from one type of storm to another. The use of more complete characterizations of early storm structure (e.g., as obtained from scanning Doppler radars), coupled with more sophisticated initialization and assimilation pro-

cedures, may lead to improved predictions, although such experiments are only now being attempted (e.g., Lin et al. 1990).

We are extending the simulations described here to a broader parameter space that includes rectilinear hodographs, as well as systematic changes in the CAPE and mean shear, in an effort to better characterize storm behavior and provide more specific guidance for using the SREH as a nowcasting or forecasting parameter.

Acknowledgments. The numerical simulations were performed on the Cray X-MP at the National Center for Atmospheric Research [which is sponsored by the National Science Foundation (NSF)] and on the Cray-2 at the National Center for Supercomputing Applications, University of Illinois. Additional computer support was provided by the Geosciences Computer Network (GCN) at the University of Oklahoma and by the National Severe Storms Laboratory. The authors are grateful to Wes Roberts, Jay Davis, and Dwight Moore of the GCN for help with data analysis and graphics packages, and to Sue Weygandt for skillfully drafting the figures. Comments provided by W. Martin and C. Hane of the National Severe Storms Laboratory, and especially those by anonymous reviewers, greatly improved the quality of the manuscript. This research represents part of the second author's M.S. thesis at the School of Meteorology, University of Oklahoma, and was supported by the National Science Foundation under Grants ATM86-57013 and ATM88-15371 to the first author. The initial draft of this paper was completed while the first author was a visiting sabbatical fellow at the Army High Performance Computing Research Center (AHPCRC), University of Minnesota. This visit was supported by the Army Atmospheric Sciences Laboratory through a supplemental grant to the Center for Analysis and Prediction of Storms, University of Oklahoma, the latter of which is funded by the NSF through Grant ATM88-09862. The Minnesota AHPCRC is funded in part by the U.S. Army Research Office under Contract DAAL03-89-C-0038.

APPENDIX

Analytical Formula for the SREH

Given a suitable model of storm motion, here the 0–12-km density-weighted base-state winds, or observed storm motion, one can readily compute the storm-relative environmental helicity (SREH) for our analytical wind profiles, which are defined by

$$u(z) = -R\cos\left(\frac{\beta z}{\chi}\right), \qquad 0 \leq z \leq \chi$$
$$v(z) = R\sin\left(\frac{\beta z}{\chi}\right)$$

and

$$u(z) = -R\cos\beta, \qquad \chi \leq z, \tag{A1}$$
$$v(z) = R\sin\beta$$

where β is the angle (°) through which the ground-relative winds turn from $z = 0$ to $z = \chi$ (the top of the shear layer) and R is the hodograph radius (Fig. A1). An equation for the 0–3-km storm-relative environmental helicity may be obtained as follows. Helicity is minus twice the signed area swept out by the wind vector on a wind hodograph (Davies-Jones et al. 1990). [An area is positive (negative) if it is swept out counterclockwise (clockwise).] Therefore, the 0–3-km ground-relative environmental helicity H_0 is given simply by

$$H_0 = R^2\alpha, \tag{A2}$$

where α is the angle (rad), measured in the clockwise direction, of the ground-relative wind vectors from the surface to 3 km (Fig. A1). The helicity relative to a reference frame moving with velocity (U, V) is given by

$$H = H_0 - [-2A(\Delta OST)] + [-2A(\Delta MST)], \tag{3}$$

where $A(\Delta OST)$ denotes the signed area of triangle OST, etc. (Note that the area of triangle OST is negative for the current hodographs.) The signed area A of a triangle defined by any three points u_i, v_i, $i = 1$, 2, 3, on a wind hodograph is given by

$$A = \frac{(u_1v_2 - u_2v_1 + u_2v_3 - u_3v_2 + u_3v_1 - u_1v_3)}{2}. \tag{A4}$$

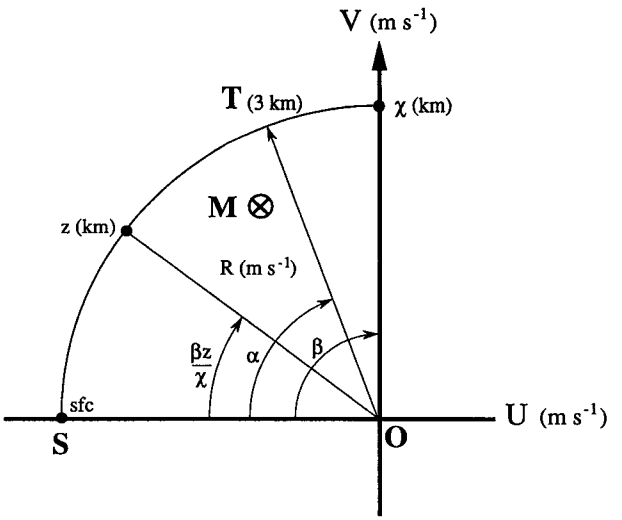

FIG. A1. Schematic hodograph used to derive the analytical formula for the SREH. The idealized vertical wind profile is shown by the thin solid arc, next to which are labeled points defining the surface (S), $z = 3$ km (T), and top of the shear layer (χ). The hodograph radius R is given in kilometers, and the open circle inscribed with a "×" (labeled M) defines the storm motion. Angles are as shown.

From (A3) and (A4), the helicity in the moving reference frame is

$$H = R^2\alpha + RU\sin\alpha - RV[1 - \cos\alpha]. \quad \text{(A5)}$$

The SREH and mean-wind helicity are determined by substituting the actual storm motion and the 0–12-km density-weighted mean wind, respectively, for (u, v) in (A4). The density-weighted mean wind $(\bar{u}, \bar{v})$ in the layer from $z = 0$ to $h(=12$ km) is calculated by approximating the ambient density by $\rho = \rho_0 e^{-\lambda z}$, where λ^{-1} ($\approx$9.7 km) is an appropriate scale height, and by using the following expression derived from (A1):

$$\bar{u} = \frac{R}{1 - e^{-\lambda h}}\left\{\frac{\lambda}{\lambda^2 + \beta^2/\chi^2}\left[e^{-\lambda\chi}\left(\lambda\cos\beta - \frac{\beta}{\chi}\sin\beta\right) - \lambda\right] - \cos\beta[e^{-\lambda\chi} - e^{-\lambda h}]\right\}$$

$$\bar{v} = \frac{R}{1 - e^{-\lambda h}}\left\{\frac{\lambda}{\lambda^2 + \beta^2/\chi^2}\left[-e^{-\lambda\chi}\left(\lambda\sin\beta + \frac{\beta}{\chi}\cos\beta\right) + \frac{\beta}{\chi}\right] + \sin\beta[e^{-\lambda\chi} - e^{-\lambda h}]\right\}. \quad \text{(A6)}$$

REFERENCES

André, J. C., and M. Lesieur, 1977: Influence of helicity on the evolution of isotropic turbulence at high Reynolds number. *J. Fluid. Mech.*, **88,** 187–207.

Brandes, E. A., R. P. Davies-Jones, and B. C. Johnson, 1988: Streamwise vorticity effects on supercell morphology and persistence. *J. Atmos. Sci.*, **45,** 947–963.

Brooks, H. E., 1992: Operational implications of the sensitivity of modelled thunderstorms to thermal perturbations. Preprints, *Fourth AES/CMOS Workshop on Operational Meteorology,* Atmospheric Environment Service/Canadian Meteorological and Oceanographic Society, Whistler, British Columbia, 10 pp.

——, C. A. Doswell III, and R. Davies-Jones, 1993: Environmental helicity and the maintenance and evolution of low-level mesocyclones. *Frontiers in Tornado Research,* C. R. Church, Ed., American Geophysical Union Press, in press.

Browning, K. A., 1962: Cellular structure of convective storms. *Meteor. Mag.*, **91,** 341–350.

——, 1964: Airflow and precipitation trajectories within severe storms that move to the right of the winds. *J. Atmos. Sci.*, **21,** 634–639.

——, J. C. Fankhauser, J.-P. Chalon, P. J. Eccles, R. C. Strauch, F. H. Merrem, D. J. Musil, E. L. May, and W. R. Sand, 1976: Structure of an evolving hailstorm. Part V: Synthesis and implications for hail growth and hail suppression. *Mon. Wea. Rev.*, **104,** 603–610.

Davies, J. M., 1989: On the use of shear magnitudes and hodographs in tornado forecasting. Preprints, *12th Conf. on Weather Forecasting and Analysis,* Monterey, CA, Amer. Meteor. Soc., 219–224.

Davies-Jones, R. P., 1984: Streamwise vorticity: the origin of updraft rotation in supercell storms. *J. Atmos. Sci.*, **41,** 2991–3006.

——, and J. H. Henderson, 1975: Updraft properties deduced statistically from rawinsondings. *Pure Appl. Geophys.*, **113,** 787–801.

——, and H. Brooks, 1993: Mesocyclogenesis from a theoretical perspective. *Frontiers in Tornado Research,* C. R. Church, Ed., American Geophysical Union Press, in press.

——, R. Rabin, and K. Brewster, 1984: A short-term forecast model for thunderstorm rotation. *Proc., Nowcasting-II Symp.* (ESA SP-208), Norrkoping, Sweden, European Space Agency, 367–371.

——, D. W. Burgess, and M. Foster, 1990: Test of helicity as a forecast parameter. Preprints, *16th Conf. on Severe Local Storms,* Kananaskis Park, Alberta, Amer. Meteor. Soc., 588–592.

Fujita, T. T., 1965: Formation and steering mechanisms of tornado cyclones and associated hook echoes. *Mon. Wea. Rev.*, **93,** 67–78.

Johnson, B. C., and E. A. Brandes, 1986: A study of barrier effects and shed eddy phenomenon associated with supercells. Preprints, *23rd Conf. on Radar Meteorology and Conf. on Cloud Physics,* Snowmass, CO, Amer. Meteor. Soc., J65–J68.

Kerr, R. M., 1987: Histograms of helicity and strain in numerical turbulence. *Phys. Rev. Lett.*, **59,** 786.

Klemp, J. B., 1987: Dynamics of tornadic thunderstorms. *Ann. Rev. Fluid Mech.*, **19,** 369–402.

——, and R. B. Wilhelmson, 1978: The simulation of three-dimensional convective storm dynamics. *J. Atmos. Sci.*, **35,** 1070–1096.

Kraichnan, R. H., 1973: Helical turbulence and absolute equilibrium. *J. Fluid Mech.*, **59,** 745–752.

Lazarus, S. M., 1990: The influence of helicity on the stability and morphology of numerically simulated storms. M.S. thesis, School of Meteorology, University of Oklahoma, 191 pp. [Available from School of Meteorology, 100 East Boyd, Norman, Oklahoma, 73019.]

——, and K. K. Droegemeier, 1990: The influence of helicity on the stability and morphology of numerically simulated storms. Preprints, *16th Conf. on Severe Local Storms,* Kananaskis Park, Alberta, Amer. Meteor. Soc., 269–274.

Lesieur, M., 1990: *Turbulence in Fluids.* 2d ed. Kluwer Academic Publishers, 412 pp.

Lilly, D. K., 1983: Dynamics of rotating thunderstorms. *Mesoscale Meteorology—Theories, Observations, and Models.* D. Lilly and T. Gal-Chen, Eds., Reidel, 531–543.

——, 1986a: The structure, energetics and propagation of rotating convective storms. Part I: Energy exchange with the mean flow. *J. Atmos. Sci.*, **43,** 113–125.

——, 1986b: The structure, energetics and propagation of rotating convective storms. Part II: Helicity and storm stabilization. *J. Atmos. Sci.*, **43,** 126–140.

——, 1990: Numerical prediction of thunderstorms—Has its time come? *Quart. J. Roy. Meteor. Soc.*, **116,** 779–798.

Lin, Y., P. S. Ray, and K. W. Johnson, 1990: Simulation of a convective storm using Doppler radar-derived initial fields. Preprints, *16th Conf. on Severe Local Storms,* Kananaskis Park, Alberta, Amer. Meteor. Soc., 500–503.

Mandelbrot, B., 1983: *The Fractal Geometry of Nature.* W.H. Freeman and Co., 468 pp.

Marwitz, J. D., 1972a: The structure and motion of severe hailstorms. Part I: Supercell storms. *J. Appl. Meteor.*, **11,** 166–179.

——, 1972b: The structure and motion of severe hailstorms. Part II: Multi-cell storms. *J. Appl. Meteor.*, **11,** 180–188.

McCaul, E. W., Jr., 1987: Observations of the hurricane "Danny" tornado outbreak of 16 August 1985. *Mon. Wea. Rev.*, **115,** 1206–1223.

——, 1991: Buoyancy and shear characteristics of hurricane-tornado environments. *Mon. Wea. Rev.*, **119,** 1954–1978.

McPherson, R. A., 1991: Predictability experiments of a numerically-modeled supercell storm. M.S. thesis, School of Meteorology, University of Oklahoma, 128 pp. [Available from School of Meteorology, 100 East Boyd, Norman, Oklahoma, 73019.]

——, and K. K. Droegemeier, 1991: Numerical predictability experiments of the 20 May 1977 Del City, OK, supercell storm. Preprints, *Ninth Conf. on Numerical Weather Prediction,* Denver, Amer. Meteor. Soc., 734–738.

Moffatt, H. K., 1985: Magnetostatic equilibria and analogous Euler flows of arbitrarily complex topology. Part I. Fundamentals. *J. Fluid. Mech.*, **159,** 359–378.

——, and A. Tsinober, 1992: Helicity in laminar and turbulent flow. *Ann. Rev. Fluid Mech.*, **24,** 281–312.

Newton, C. W., and J. C. Fankhauser, 1964: On the movements of convective storms, with emphasis on size discrimination in relation to water-budget requirements. *J. Appl. Meteor.*, **3,** 651–668.

Pelz, R. B., I. Shtilman, and A. Tsinober, 1986: On the helical nature of enforced turbulent flows. *Phys. Fluids,* **29,** 3506–3508.

——, V. Yakhot, S. A. Orszag, L. Shtilman, and E. Levich, 1985: Velocity–vorticity patterns in turbulent flow. *Phys. Rev. Lett.*, **54,** 2505–2508.

Rasmussen, E. N., and R. B. Wilhelmson, 1983: Relationships between storm characteristics and 1200 GMT hodographs, low-level shear, and stability. Preprints, *13th Conf. Severe Local Storms,* Tulsa, Amer. Meteor. Soc., J5–J8.

Rotunno, R., and J. B. Klemp, 1982: The influence of the shear-induced pressure gradient on thunderstorm motion. *Mon. Wea. Rev.*, **110,** 136–151.

——, and ——, 1985: On the rotation and propagation of simulated supercell storms. *J. Atmos. Sci.*, **42,** 271–292.

Tsinober, A., 1990: Turbulent drag reduction versus structure of turbulence. *Structure of Turbulence and Drag Reduction,* A. Gyr, Ed., Springer-Verlag, 313–340.

Vasiloff, S. V., E. A. Brandes, R. P. Davies-Jones, and P. S. Ray, 1986: An investigation of the transition from multicell to supercell storms. *J. Climate Appl. Meteor.*, **25,** 1022–1036.

Walko, R. L., 1993: Tornado spin-up beneath a convective cell: Required basic structure of the near-field boundary-layer winds. *Frontiers in Tornado Research,* C. R. Church, Ed., American Geophysical Union Press, in press.

Wallace, J. M., and J.-L. Balint, 1990: An experimental study of helicity and related properties in turbulence flows. *Topological Fluid Mechanics,* H. K. Moffatt and A. Tsinober, Eds., Cambridge University Press, 585–597.

Weaver, J. F., 1979: Storm motion as related to boundary layer convergence. *Mon. Wea. Rev.*, **107,** 612–619.

Weisman, M. L., and J. B. Klemp, 1982: The dependence of numerically simulated convective storms on vertical wind shear and buoyancy. *Mon. Wea. Rev.*, **110,** 504–520.

——, and ——, 1984: The structure and classification of numerically simulated convective storms in directionally varying wind shears. *Mon. Wea. Rev.*, **112,** 2479–2498.

——, and ——, 1986: Characteristics of isolated convective storms. *Mesoscale Meteorology and Forecasting,* P. Ray, Ed., Amer. Meteor. Soc., 331–358.

Wilhelmson, R. B., and J. B. Klemp, 1978: A three-dimensional numerical simulation of storm splitting that leads to long-lived storms. *J. Atmos. Sci.*, **35,** 1974–1986.

——, and C.-S. Chen, 1982: A simulation of the development of successive cells along a cold outflow boundary. *J. Atmos. Sci.*, **39,** 1466–1483.

Woodall, G. R., 1990: Qualitative analysis and forecasting of tornadic activity using storm-relative environmental helicity. NOAA Tech. Memo. NWS SR-127, 57 pp. [Available from National Technical Information Service, 2585 Port Royal Road, Springfield, VA 22151.]

Wu, W.-S., D. K. Lilly, and R. M. Kerr, 1992: Helicity and thermal convection with shear. *J. Atmos. Sci.*, **49,** 1800–1809.